Mon. Not. R. Astron. Soc. **000**, 1–27 (2016) Printed 4 April 2016 (MN LATEX style file v2.2)

ISM gas studies towards the TeV PWN HESS J1825-137 and northern region.

F.Voisin[1⋆], G.Rowell[1], M.G.Burton[2], A.Walsh[3], Y.Fukui[4], F.Aharonian[5,6]
[1] *School of Physical Science, Adelaide university, North Terrace , Adelaide , SA 5005, Australia*
[2] *School of Physics, University of New South Wales, Sydney, NSW 2052, Australia*
[3] *International Centre for Radio Astronomy Research, Curtin University, GPO Box U1987, Perth WA 6845, Australia*
[4] *Department of Physics, University of Nagoya, Furo-cho, Chikusa-ku, Nagoya, 464-8601, Japan*
[5] *Max-Planck-Institut für Kernphysik, P.O. Box 103980, D-69029 Heidelberg, Germany*
[6] *Dublin Institute for Advanced Studies, 31 Fitzwilliam Place, Dublin 2, Ireland*

arXiv:1604.00090v1 [astro-ph.HE] 1 Apr 2016

4 April 2016

ABSTRACT

HESS J1825−137 is a pulsar wind nebula (PWN) whose TeV emission extends across ~ 1 deg. Its large asymmetric shape indicates that its progenitor supernova interacted with a molecular cloud located in the north of the PWN as detected by previous CO Galactic survey (e.g Lemiere, Terrier & Djannati-Ataï 2006).

Here we provide a detailed picture of the ISM towards the region north of HESS J1825−137, with the analysis of the dense molecular gas from our 7mm and 12mm Mopra survey and the more diffuse molecular gas from the Nanten CO(1–0) and GRS ^{13}CO(1–0) surveys. Our focus is the possible association between HESS J1825−137 and the unidentified TeV source to the north, HESS J1826−130. We report several dense molecular regions whose kinematic distance matched the dispersion measured distance of the pulsar. Among them, the dense molecular gas located at (RA, Dec)=(18.421h,−13.282°) shows enhanced turbulence and we suggest that the velocity structure in this region may be explained by a cloud-cloud collision scenario.

Furthermore, the presence of a Hα rim may be the first evidence of the progenitor SNR of the pulsar PSR J1826–1334 as the distance between the Hα rim and the TeV source matched with the predicted SNR radius $R_{\rm SNR} \sim 120$ pc.

From our ISM study, we identify a few plausible origins of the HESS J1826−130 emission, including the progenitor SNR of PSR J1826−1334 and the PWN G018.5−0.4 powered by PSR J1826−1256. A deeper TeV study however, is required to fully identify the origin of this mysterious TeV source.

Key words: molecular data – pulsars: individual: PSR J1826−1334 – ISM: clouds – cosmic-rays – gamma-rays: ISM.

1 INTRODUCTION

HESS J1825−137 is one of the brightest and most extensive pulsar wind nebulae (PWNe) detected in TeV γ-rays (Aharonian et al. 2006). It is powered by the high spin-down power ($\dot{E}_{\rm SD} = 2.8 \times 10^{36}$ erg/s) pulsar PSR J1826−1334 with a dispersion measure distance of 3.9±0.4 kpc and characteristic age $\tau_c \sim 20$ kyr.

PWNe represent a significant fraction of the Galactic TeV γ-ray source population. They convert a varying fraction of their pulsars' spin down energy $\dot{E}_{\rm SD}$ into high energy electrons. The electron flow is temporally randomized and re-accelerated at a termination shock resulting from pressure from the surrounding interstellar medium (ISM). Inverse-Compton (IC) up-scattering of soft photons then leads to TeV γ-rays, and associated synchrotron radio to X-ray emission.

The morphology of PWNe can be heavily influenced by the ISM. The interaction of the progenitor supernova shock with adjacent molecular clouds can lead to a reverse shock propagating back into the PWN (Blondin, Chevalier & Frierson 2001), giving rise to an asymmetry in the radio, X-ray and γ-ray emission that can trail away from the pulsar along the pulsar-molecular cloud axis.

HESS J1825−137 is an excellent example of this situa-

⋆ E-mail: fabien.voisin@adelaide.edu.au (AVR); fabien.voisin@adelaide.edu.au(ANO)

tion. The morphology of HESS J1825−137 (Fig. 1) displays a clear asymmetry with respect to PSR J1826−1334, and a molecular cloud to the north revealed by Lemiere, Terrier & Djannati-Ataï (2006), with the bulk of the TeV γ-ray extending up to a degree south of the pulsar.

Interestingly, the weak TeV γ-ray emission component to the north labeled HESS J1826−130 (Deil et al. 2015) appears to spatially overlap this northern molecular cloud (see Fig. 1). Such an overlap could result from the interaction of multi-TeV cosmic-rays with molecular clouds, and thus raises the possibility of cosmic-ray acceleration in the vicinity, notably from HESS J1825-137's progenitor SNR.

We also note the presence of two additional SNRs in the region : G018.1−0.1 and G018.6−0.2 (Brogan et al. 2006) as shown in Fig. 1. Ray et al. (2011) also discovered the radio quiet pulsar PSR J1826-1256 (P2 in Fig. 1) with a spin down luminosity $\dot{E}_{\rm SD} = 3.6 \times 10^{36}$ erg s^{-1}, a period $P = 100$ ms and a characteristic age $\tau_c = 13$ kyr and powering the PWN G018.5–0.4 observed in X-rays by Roberts et al. (2007) . Although no dispersion measure could be derived, Wang (2011) argues that the pulsar is located at a distance $d = 1.2 - 1.4$ kpc. Consequently, it is possible each of these sources could also contribute to the TeV emission inside HESS J1826−130.

To further investigate this issue, higher resolution mapping (improving that of the $8'$ resolution of the CO(1–0) data used by Lemiere, Terrier & Djannati-Ataï 2006) of the molecular cloud and surrounding region is needed to probe the density and dynamics of the gas. In this paper, we made use of CO, and ^{13}CO survey data (from the Nanten telescope and the Galactic Ring Survey - GRS) plus new mapping of dense gas tracers such as carbon monosulphide (CS) and ammonia (NH_3) with the Mopra telescope in Australia.

In section §2, we review the properties of the Mopra and Nanten telescopes, and the GRS as well as the methodology used to reduce our Mopra observations. Then, in section §3, we briefly introduce the different gas tracers that we detected towards HESS J1826−130 and their physical properties. We present the results of our observations and provide gas parameter estimates for various regions using our CO, CS and NH_3 analysis in section §4. Finally, in section §5, we discuss the dynamics of the dense gas and finally discuss a few possible counterparts to the HESS J1826−130 emission.

2 DATA OBSERVATION AND REDUCTION

2.1 Mopra

We observed a $60' \times 60'$ region (large red dashed box in Fig. 1) centred at (RA,Dec)=(18.425h,−13.3°) in the 12mm band from the 19$^{\rm th}$ to the 27$^{\rm th}$ of January 2012 with the 22 metre Mopra telescope. We combined our observations with the HOPS survey (Walsh et al. 2011), which covered the Galactic plane within the Galactic latitude b=-0.5 to b=0.5 to achieve better sensitivity (see Table 1). Additionally, we observed a $40' \times 40'$ subsection (small red dashed box in Fig. 1) centred at (RA,Dec)=(18.427h,−13.17°) in the 7mm band. Four 7mm ON-OFF switched deep pointings were taken at (RA,Dec)=(18.419h,−13.38°), (18.423h,−13.34°), (18.419h,−13.31°) and (18.420h,−13.27°) from the 13$^{\rm th}$ until the 21$^{\rm st}$ of April to search for additional emission from the isotopologue C^{34}S(1–0). Unfortunately, our observations were not sensitive enough to detect such emission. Finally, another 7mm deep pointing was taken in August 2014 towards the position (RA,Dec)=(18.419h,−14.04°) towards a molecular cloud south of HESS J1825−137.

For these observations, we used the Mopra spectrometer MOPS in 'zoom' mode, which allowed the recording of sixteen sub-bands, each consisting of 4096 channels and a 137.5 MHz bandwidth, simultaneously. The Mopra OTF mapping fully sampled the region with a beam size of $2'$ (12mm) and $1'$ (7mm), a velocity resolution of 0.4 km/s (12mm) and 0.2 km/s (7mm). For the reduction of our OTF observations, we first used `Livedata`[1] which outputs the spectra of each scan using an OFF position as reference. We used a first-order polynomial fit to subtract the baseline. Then, we used `Gridzilla` [2] to produce 3D cubes of each sub-bands in antenna temperature T_A^* (K) as a function of RA, Dec and line of sight velocity. We used a $15''$ grid to map our region and the data were finally smoothed via a Gaussian with $1.25'$ FWHM in order to smooth out fluctuations. The $T_{\rm rms}$/channel of each map in which detections have been found are listed in Table 1.

Finally, we used the `ASAP`[3] software to reduce our ON-OFF deep pointing observations. The OFF position measurement was used to obtain the antenna temperature T_A^* of each scans. The achieved $T_{\rm rms}$/channel ranges from 0.05 to 0.1 K. The beam temperature $T_{\rm mb}$ of maps and ON/OFF pointings were obtained using the main beam conversion factor $\eta_{\rm mb}$ determined by Urquhart et al. (2010) (see Appendix A).

2.2 Nanten and GRS

To probe the more extended diffuse gas, we made use of more recent CO observations. The 4 m Nanten telescope carried out a CO(1–0) survey over the Galactic plane with a $2.6'$ beam size and a sampling grid of $4'$, a velocity resolution Δv=1.0 km/s (Mizuno & Fukui 2004) and a typical $T_{\rm rms}$/channel value of $\sim$ 0.35K. The Galactic Ring Survey ^{13}CO(1–0) (GRS) mapped the Galactic ring in our Galaxy using the Five College Radio Astronomy Observatory (FCRAO). It has a beam FWHM of $44''$, a sampling grid of $22''$, a velocity resolution Δv ∼0.2 km/s and an averaged $T_{\rm rms}$/channel∼ 0.36K (Jackson 2004).

3 OVERVIEW OF DETECTED LINES

Table 1 indicates the various spectral lines detected in our analysis of Mopra data. The following sections review the properties of the major spectral tracers.

3.1 Carbon monosulfide CS(1-0) and isotopologues

A major 7mm line in our study is the J=1–0 emission from the carbon monosulfide (CS) molecule. CS is commonly

[1] http://www.atnf.csiro.au/computing/software/livedata/
[2] http://www.atnf.csiro.au/computing/software/Gridzilla/
[3] http://svn.atnf.csiro.au/trac/asap

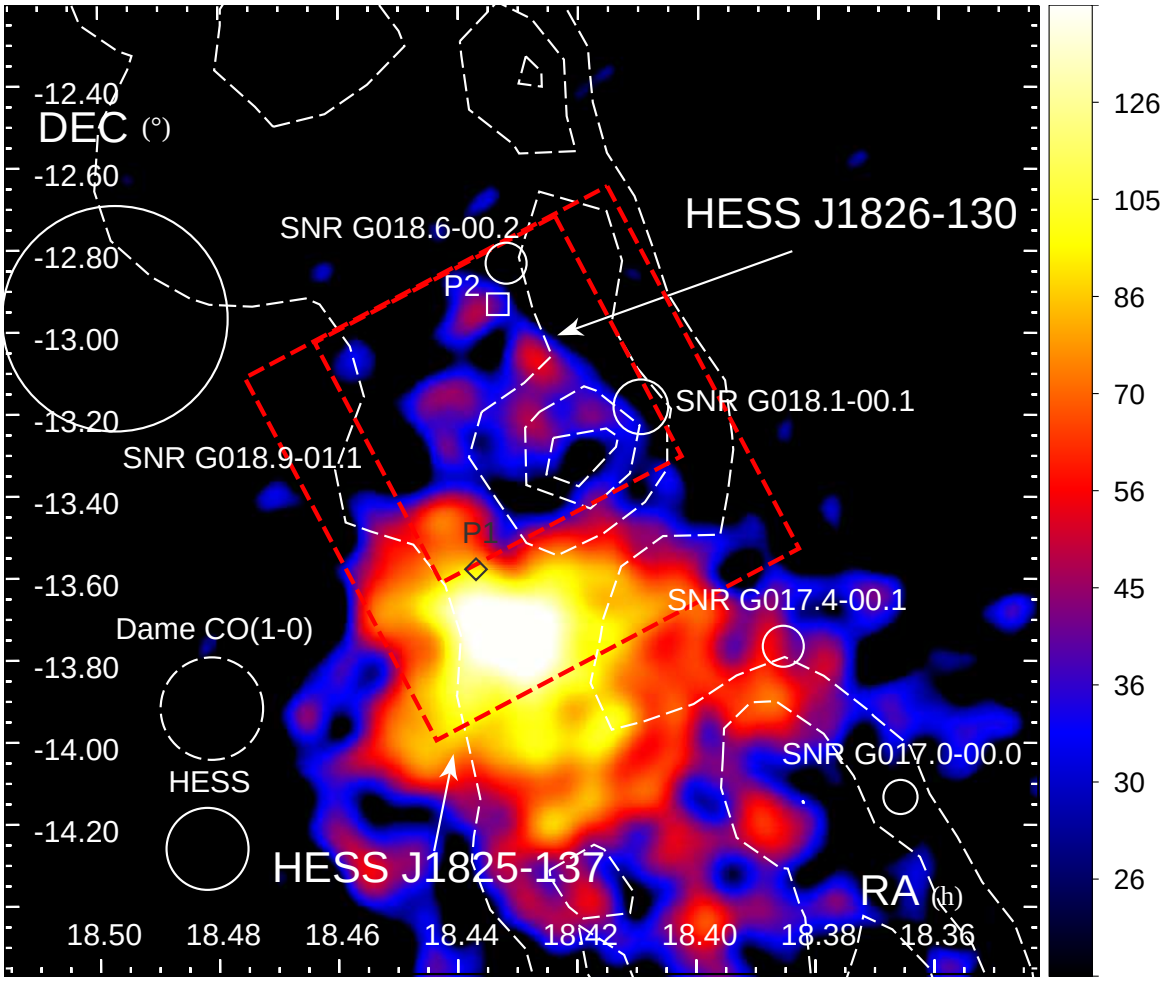

Figure 1. HESS excess counts image (> 100 GeV) towards HESS J1825−137 overlaid by the CO(1–0) integrated intensity contour (40, 60, 80, 100 K km/s) between $v_{\rm lsr} = 40 - 60$ km/s from Dame, Hartmann & Thaddeus (2001) as revealed by Lemiere, Terrier & Djannati-Ataï (2006). The white circles represent the different SNRs detected (Brogan et al. 2006). P1 indicates the pulsar PSR J1826-1334's location while P2 shows the position of PSR J1826–1256. The small and large red dashed boxes (see online version) represent our 7mm and 12mm Mopra coverage respectively.

found inside dense cores. Its critical density ,n_c, at $T_{\rm k}$=10K is $\sim 2 \times 10^4$ cm^{-3} and thus allows study of dense clumps located inside molecular clouds. The isotopologues of CS namely C^{34}S, and C^{13}S are generally assumed to be optically thin given their abundance ratio [CS]/[C^{34}S]∼24 and [CS]/[^{13}CS]∼75 based on terrestrial measurements (see e.g Frerking et al. 1980). Their detection can provide estimates of optical depth and thus robust mass estimates of dense cores.

3.2 Ammonia NH_3

Ho & Townes (1983) outlined the properties of the ammonia molecule. The NH_3(J,K) structure consists of ladders where J is the total momentum and K is the momentum from the quadrupole axis. Only energy states where J=K are metastable and thus can be populated easily. NH_3(1,1) spectra consist of one main line surrounded by four satellite lines whose expected relative strength compared to the main component is ∼ 25%. However, the ratio depends on optical depth, and so this enables an efficient estimation of the dense molecular gas opacity. Finally, the relative strength of the NH_3(2,2) and NH_3(3,3) satellite lines relative to their main components are ∼5% and ∼3% respectively and it is therefore unlikely to detect these satellite lines.

3.3 SiO(1-0)

Silicates can be released from dust grains into the gas phase from the crossing of a weak shock inside the molecular clouds (Schilke et al. 1997; Gusdorf et al. 2008). Silicon monoxide is then produced behind the shock and the non vibrational SiO(1–0,v=0) emission can be detected. Its detection be-

Table 1. List of all gas tracers detected during our Mopra 7 and 12 mm observations towards HESS J1826−130, their respective rest frequencies, and the achieved mapping $T_{\rm rms}$ of the data cubes where these emission are found.

Tracer	Frequency (GHz)	$T_{\rm rms}$ (K/channel)
7mm		
SiO(1–0,v=2)	42.820582	0.05
SiO(1–0,v=0)	43.423864	0.05
$CH_3OH(7_0–6_1)$	44.069476	0.06
H51α	45.453720	0.06
HC_3N(5–4,F=4-3)	46.247580	0.06
$C^{34}S$(1–0)	48.206946	0.08
CS(1–0)	48.990957	0.08
12mm		
H69α	19.591110	0.05
H65α	23.404280	0.05
NH_3(1,1)	23.594470	0.05
NH_3(2,2)	23.722634	0.05
NH_3(3,3)	23.870127	0.05
H62α	26.939170	0.05

comes optimal for a shock speed $v_{\rm s} = 25 - 50\,$km/s and a target density $n_{\rm H} = 10^4$ cm^{-3} (Gusdorf et al. 2008). Our 7mm settings also enabled a search for SiO(1–0,v=1 to 3), and their non vibrational isotopologues ^{29}SiO(1–0,v=0) and ^{30}SiO(1–0,v=0).

3.4 Other spectral tracers

The 12mm and 7mm recombination lines H62α, H65α and H69α and H51α indicate ionized gas by UV radiation from nearby stars in HII complexes. Thus, these are important tracers of star formation and photo-dissociation regions where newborn stars radiate inside molecular clouds.

Cyanoacetylene (HC_3N) can be detected in warm molecular clouds and can be associated with star forming regions. This line emission is typically assumed optically thin and the large number of transitions available in the millimetre band allow the computation of physical parameters of molecular clouds (Morris et al. 1976).

Also, the methanol transition $CH_3OH(7_0$-$6_1)$ is a class I maser and generally traces star formation outflows. Weak shocks also tend to release CH_3OH from the grain mantle and collisionally pump the molecule from increased interaction with H_2 (see Voronkov et al. 2014 and references therein).

4 RESULTS AND ANALYSIS

4.1 Overview

Figs. 2 and 3 show the CO(1-0),^{13}CO(1-0), CS(1-0), and NH_3(1,1) integrated intensity maps over three different velocity spans.

As shown in the top panel of Fig. 4, we noticed that the velocity distribution of all detections inside the region covered by our 7mm survey mostly peaked in four velocity regions : $v_{\rm lsr} = 40\,$km/s, $v_{\rm lsr} = 45$ km/s, $v_{\rm lsr} = 50$ km/s and $v_{\rm lsr} = 68$ km/s and the ^{13}CO(1–0) emission showed distinct structures at each velocities. We identified six bright

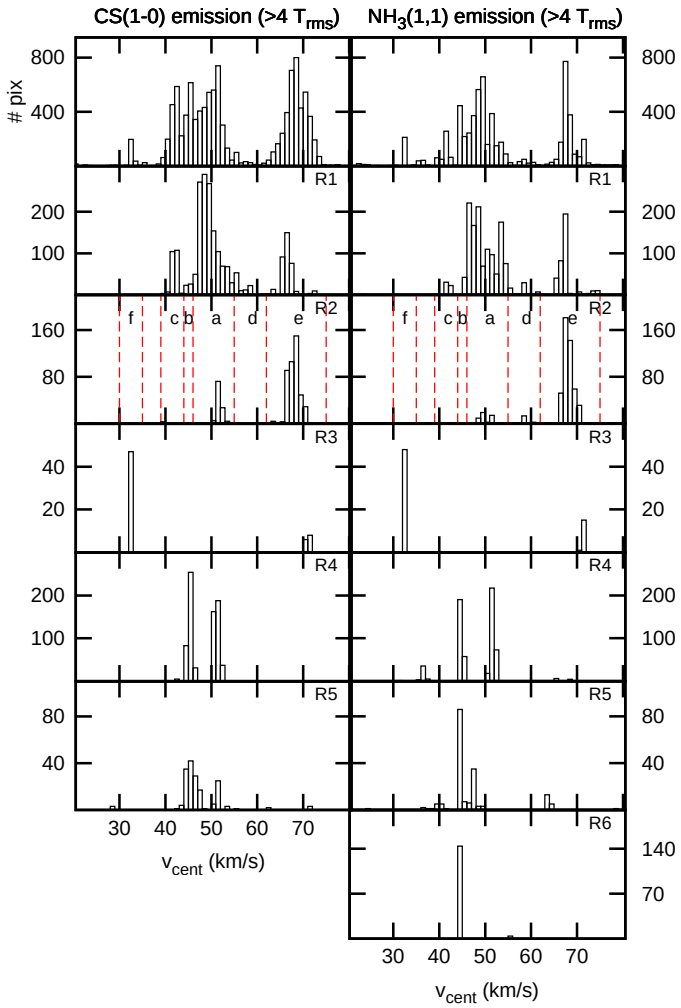

Figure 4. CS(1–0) *(left)* and NH_3(1,1) *(right)* binned centroid velocity distribution (1 km/s intervals) per pixel of the components detected above 4 $T_{\rm rms}$ towards the region covered by our 7mm survey and more specifically the regions *R1* to *R6*. The subcomponents 'a' to 'f' referring to distinct velocity groups (see text and Tables 2 and 3) are delimited by the dashed-red vertical lines (see online version).

regions, that we labelled *R1* to *R6* (see Figs. 2 and 3). Each region showed bright emission from CO, CS and NH_3 listed above (see Fig. 5 for spectral plots), with the exception of *R6* whose NH_3(1,1) averaged emission over the region was too weak. The composition of these regions will be discussed in detail in order to provide a better understanding about the complex morphology of the observed emission.

Fig. 6 shows the 8μm continuum image from the Spitzer GLIMPSE survey (Churchwell et al. 2009). We observed various infra-red (IR) features spatially coincident with dense molecular gas from some the aforementioned regions. Anderson et al. (2014) indicated that these IR sources were mostly HII regions (see red diamonds in Fig. 3). We detected several star-forming region tracers that were spatially coincident with these IR sources (which will be detailed in the next section). Association between these IR regions and the aforementioned molecular gas regions indicate likely source for driving the gas motion.

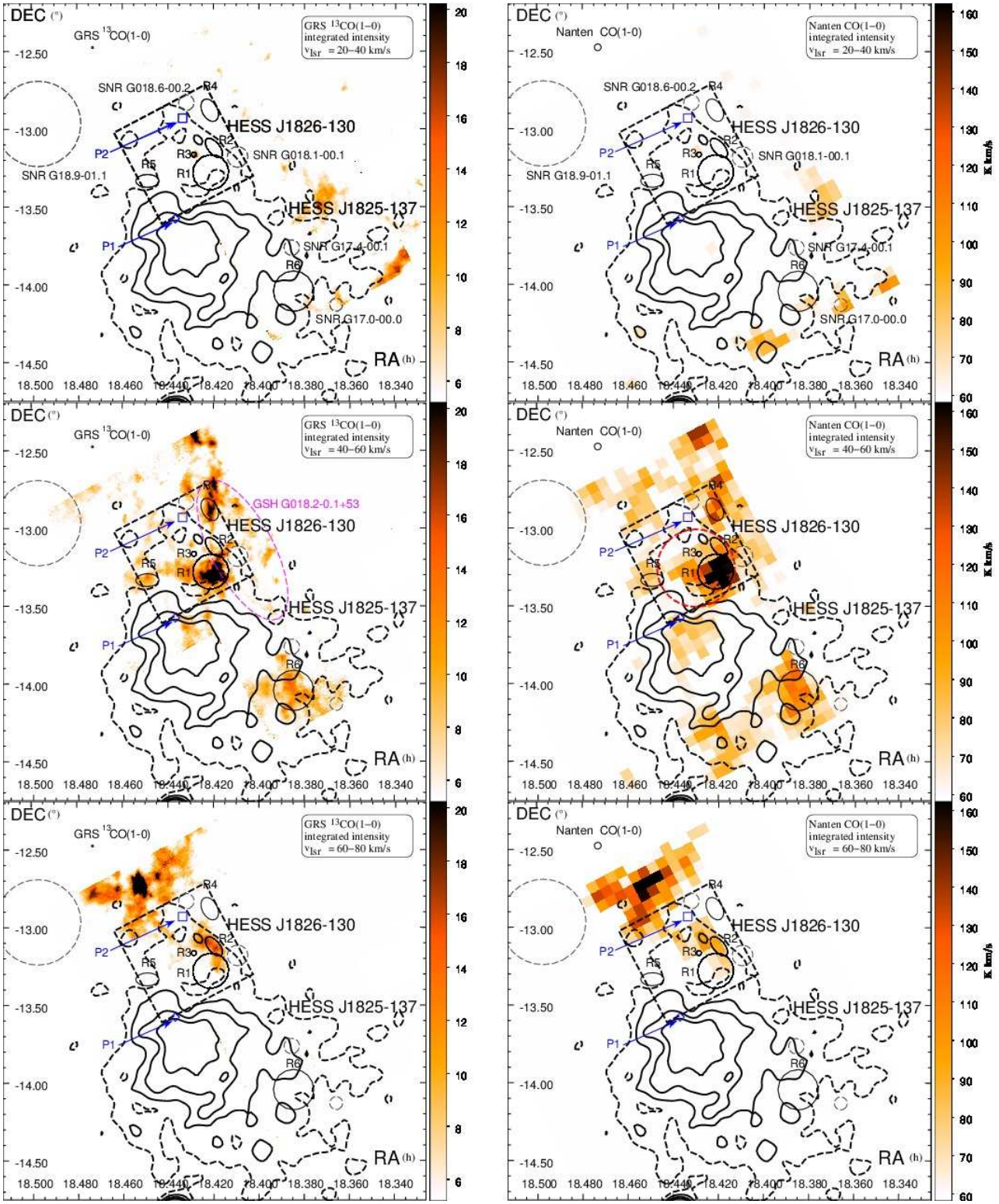

Figure 2. GRS ^{13}CO(1-0) (left) and Nanten CO(1-0) (right) integrated intensity between $v_{\rm lsr} = 20 - 40\,$km/s, $v_{\rm lsr} = 40 - 60\,$km/s and $v_{\rm lsr} = 60 - 80\,$km/s. The different black ellipses represent regions for further discussion based on detection of dense gas via the CS(1–0) and NH_3(1,1) tracers (see Fig. 3). The HESS TeV emission from HESS J1825−137 and HESS J1826−130 is shown in black contours (dashed and solid) and the surrounding SNRs are displayed in black dashed circles with their label displayed in the first panels. The region covered by our 7mm survey is shown in black dashed box. The putative molecular shell GSH 18.1-0.2+53 (Paron et al. 2013) is shown in purple dashed ellipse (see online version) in the middle-left panel. Finally, the red dashed circle in the middle right panel represents the region whose mass and density have been calculated (see section 4.2).

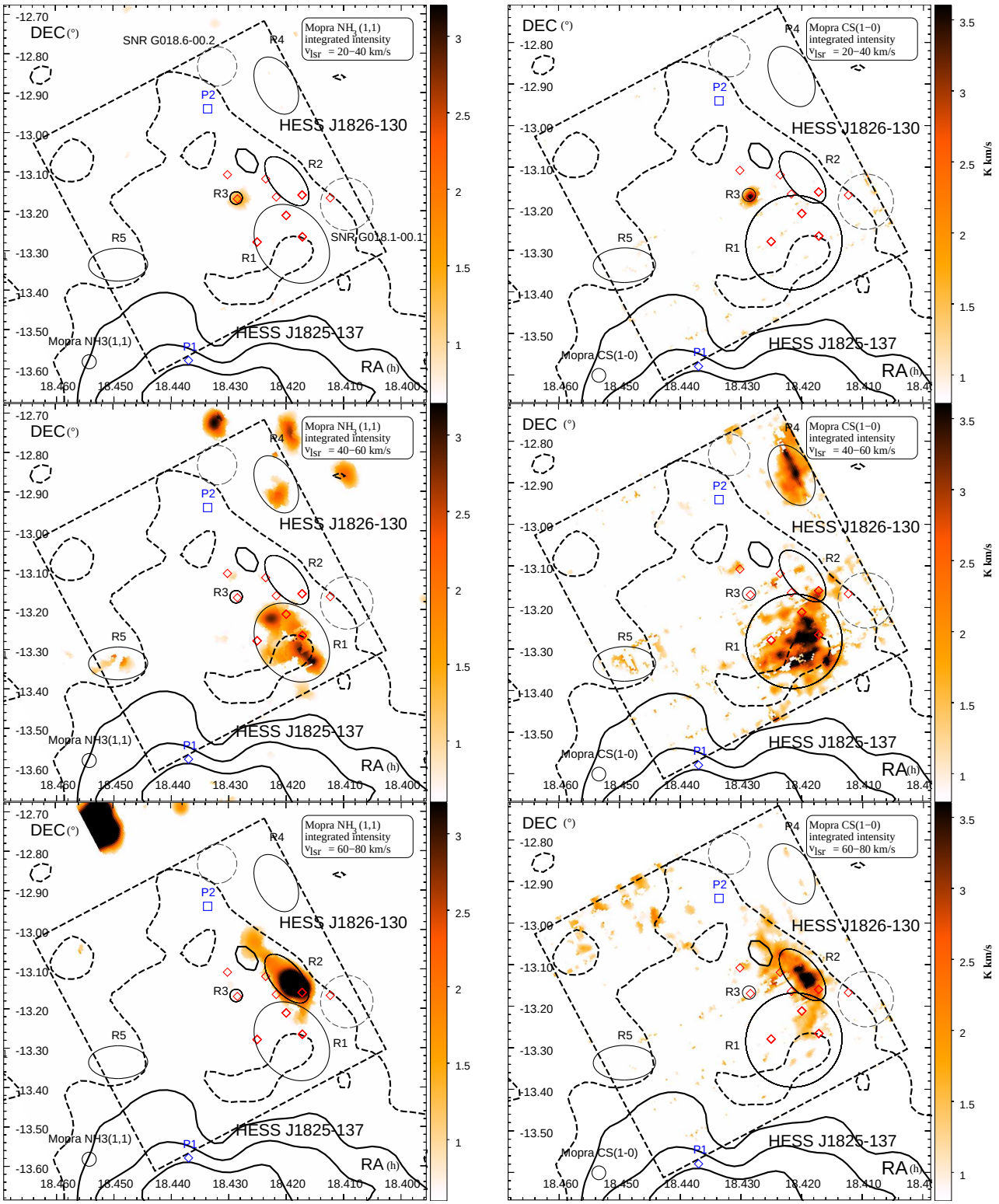

Figure 3. Mopra $NH_3(1,1)$ and CS(1–0) integrated intensity between $v_{\rm lsr} = 20 - 40\,$km/s, $v_{\rm lsr} = 40 - 60\,$km/s and $v_{\rm lsr} = 60 - 80\,$km/s overlaid by the different regions where $NH_3(1,1)$ and CS(1–0) were detected. The region covered by our 7mm survey is shown in black dashed box. The diamonds (red in colour version) indicate the different HII regions shown in the SIMBAD database (see Anderson et al. 2014 for latest HII regions catalogue) while the SNRs are shown in black dashed circles with their labels shown in the top panels.

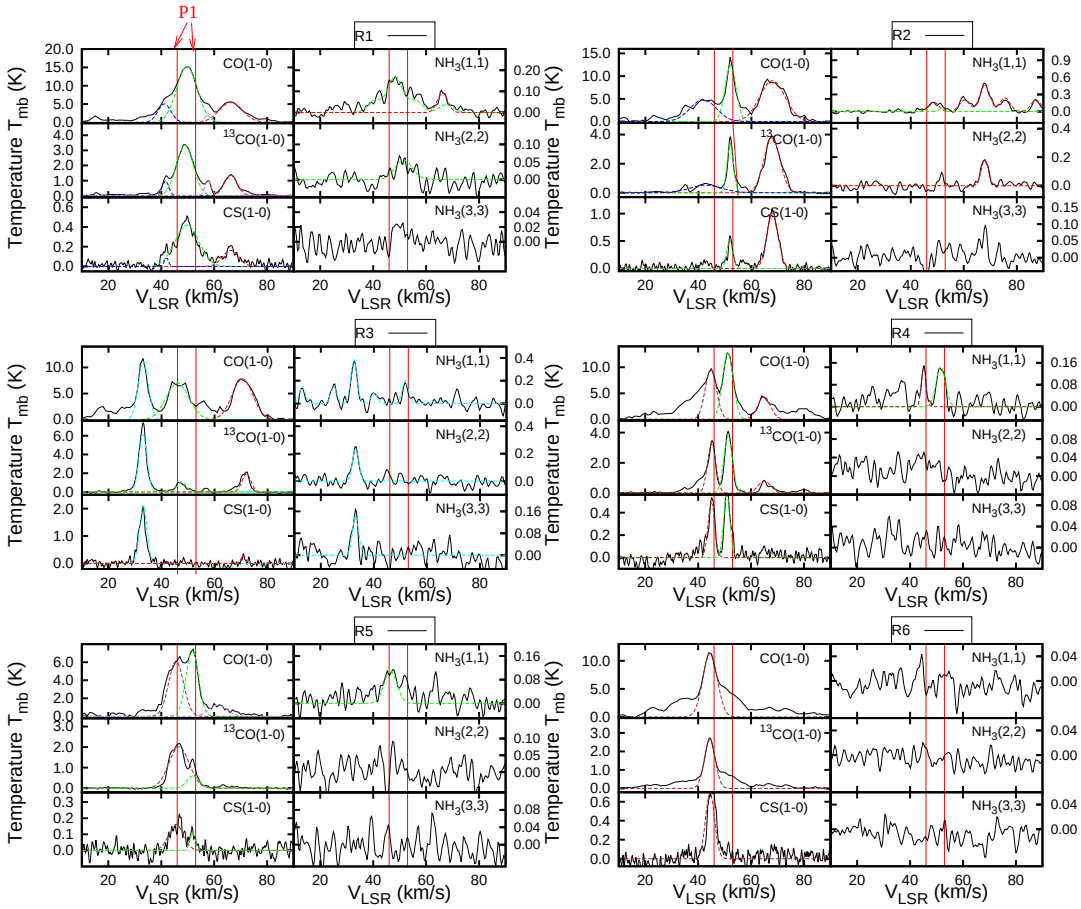

Figure 5. Averaged CO(1–0), ^{13}CO(1–0), CS(1–0) and NH_3(1,1) to (3,3) spectra for the various regions as labelled in Fig. 2 and Fig. 3. The vertical lines represent the estimated kinematic velocity range for PSR J1826–1334 (P1 in Fig. 2). Gaussian fits are represented as dashed lines whose colour code indicates the following velocity $v_{\rm lsr}$ ranges in km/s $(30-35,\ 39-44,\ 44-46,\ 46-55,\ 55-62,\ 62-75)$ = (cyan, blue, brown, green, purple, red). We emphasize that the emission located at $v_{\rm lsr}=46-55$ km/s matches the kinematic distance of pulsar P1.

4.2 CO(1–0) and ^{13}CO(1–0) analysis

The CO(1–0) and its isotopologue ^{13}CO(1–0) averaged emission in the selected regions *R1* to *R6* were fitted with a single Gaussian. The components from each region were labelled from 'a' to 'f' according to the velocity group they belonged to. For example, 'a' represents the velocity range $v_{\rm lsr}=46-55$ km/s matching the pulsar P1's kinematic distance, whilst 'b', 'c', 'd', 'e' and 'f' indicate the range $v_{\rm lsr}=44-46$ km/s, $39-44$ km/s, $55-62$ km/s, $62-75$ km/s and $30-35$ km/s respectively. The total mass was also determined using the CO(1–0) averaged integrated intensity $W_{\rm CO}$ and the conversion factor $X_{\rm CO}=2.0\times10^{20}$ cm^{-2}/(K km/s) The conversion factor is generally assumed to be constant across the Galactic plane although its value may slightly vary as a function of the galactocentric radius (Strong et al. 2004). Finally, we used a prolate geometry to provide H_2 density, $n_{\rm H_2}$, estimates via Eq. G12. The total proton density $n_{\rm H}$ can be deduced using $n_{\rm H}$=2.8 $n_{\rm H_2}$ which accounts for 20% He fraction. We also used the full width half maximum (FWHM) of the isotopologue ^{13}CO(1–0), less prone to optical depth effects (e.g broadening), to obtain the Virial mass $M_{\rm vir}$ of the selected regions. We used the inverse-squared r^{-2} and Gaussian density distribution (see Protheroe et al. 2008) as lower and upper-range of the Virial masses respectively.

Among the observed clouds, the one located at $v_{\rm lsr}=45-60$ km/s is at a kinematic distance $d=4$ kpc which is similar to that of the pulsar PSR J1826−1334, is adjacent to HESS J1825−137 (see red dashed circle in the middle right panel of Fig. 2). Assuming the molecular cloud to be spherical with radius $R_{\rm MC}\sim18$ pc and centred at (RA,Dec)=(18.431h,−13.26°), we obtain from our CO(1–0) observations an averaged density over the region $n_{\rm H}\sim6.1\times10^2$ cm^{-3} and a total mass $M_{\rm H_2}\sim3.3\times10^5M_\odot$. The density distribution is not uniform as shown by the presence of several molecular clumps (e.g as in sub-regions labeled *R1* to *R5*) seen in CO(1–0) and CS(1–0).

We also detected via the CO(1–0) and ^{13}CO(1–0) molecular transitions a diffuse molecular cloud at $v_{\rm lsr}=18$ km/s as shown in Fig. D1. Its kinematic distance $d=1.7$ kpc is similar to the pulsar PSR J1826−1256's estimated distance and it sits between the pulsar and the SNR G018.6−0.2. We derived a total mass $M_{\rm H_2}=5.3\times10^3M_\odot$ and an averaged density over the region $n_{\rm H}=5.9\times10^2$ cm^{-3} (within the red circle in Fig. D1). At

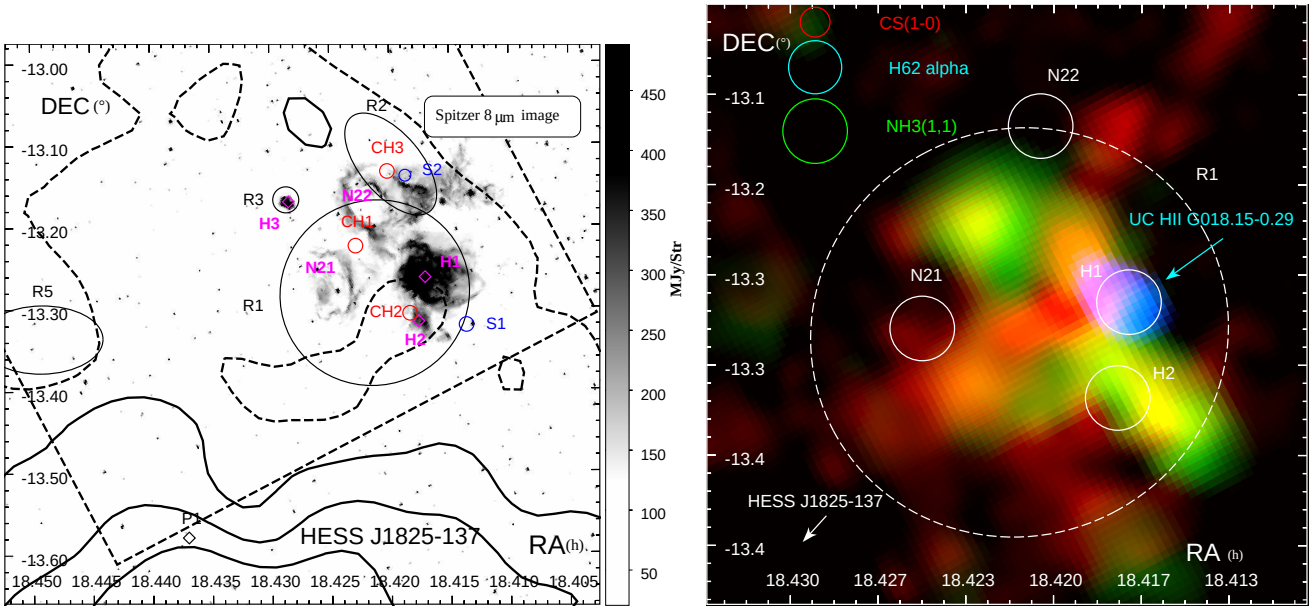

Figure 6. *(Left)* Spitzer 8μm image towards HESS J1826−130 (black contours). The red circles labelled *CH1* to *CH3* reveal the location of the 44 GHz $CH_3OH(7_1–6_0)$ emission while the blue circles (see online version) *S1* and *S2* indicate SiO(1–0,v=0) and SiO(1–0,v=2) emission. *H1* and *H2* represent the ultra-compact HII region G018.15-0.29 and the HII region G018.142-0.302 respectively (Anderson et al. 2011) while *H3* combines the HII regions G018.303-0.389 and G018.305-0.392 (White, Becker & Helfand 2005). N21 and N22 shown in purple indicate the location of two IR bubbles (Churchwell et al. 2006). The region covered by our 7mm survey is shown as a black dashed rectangle. *(Right)* Three colour image showing the CS(1–0) (red) and NH_3 (green) integrated intensity between $v_{\rm lsr} = 40 - 60$ km/s and the H62α integrated intensity (blue) between $v_{\rm lsr} = 45 - 65$ km/s towards *R1a*. The aforementioned HII regions are shown as white circles.

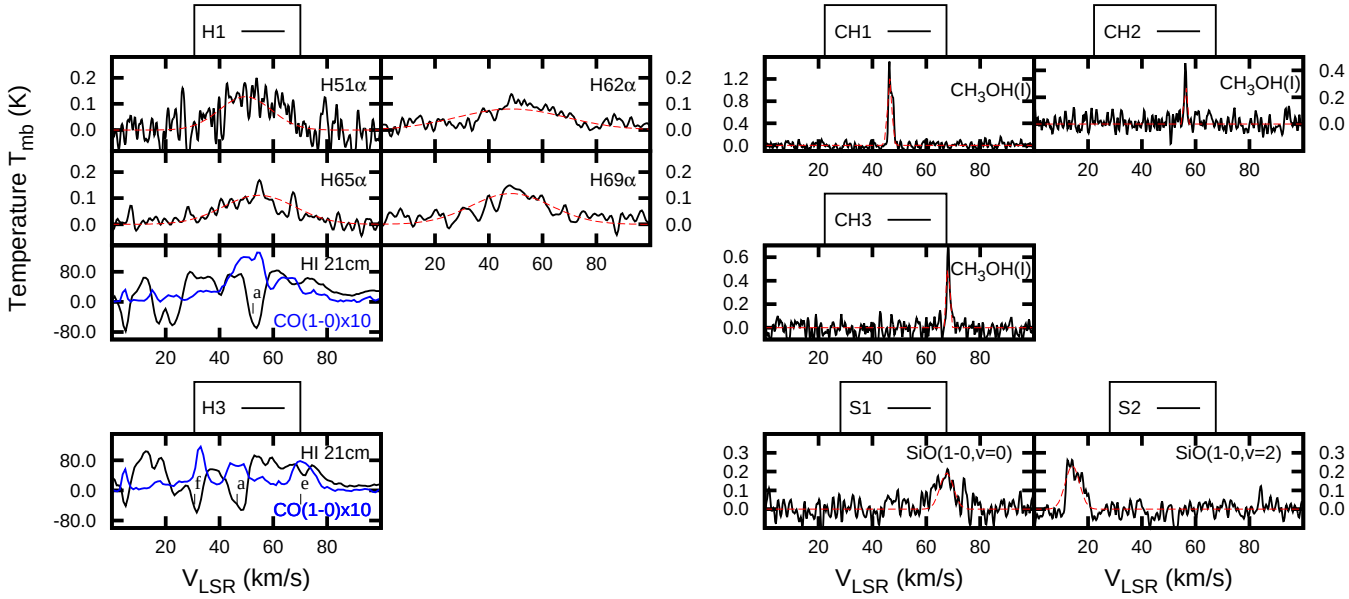

Figure 7. Spectral profile of the 44GHz maser CH_3OH(I), SiO(1–0), CO(1–0), HI 21 cm and recombination line detections from the various regions shown in Fig. 6. The dashed line (red in online version) represents the Gaussian fits to the emission. In the CO(1–0) vs HI plots, the absorptions features are indicated by black vertical lines where the labels 'a' to 'f' indicate the velocity group (see Tables 2 and 3).

$v_{\rm lsr} = 60 - 80$ km/s (see Fig. 2 bottom panel), we also observed that the molecular gas appears adjacent to the pulsar P2 and the SNR G018.6–0.2 with the bulk of the molecular gas located north of the pulsar P2.

4.3 CS analysis

From the different spectra shown in Fig. 5, CS(1–0) components were also fitted with a single Gaussian and the fit parameters have been listed in Table 2 and Table 3. In order to derive physical parameters of the different regions, we used the local thermal equilibrium assumption (LTE). In the case where the isotopologue $C^{34}S$(1–0) were also detected, we estimated of the averaged optical depth $\tau_{\rm CS(1\text{-}0)}$ using Eq. G1. An optically thin scenario $\tau_{\rm CS(1\text{-}0)}$=0 would otherwise be used to obtain the column density of the upper state $N_{\rm CS_1}$ via Eq. G2. The averaged $C^{34}S$(1–0) spectra detected in some of the studied regions *R1*,*R2*,*R3* are shown in Fig. C1.

We used the estimated kinetic temperature $T_{\rm kin}$ from our NH_3 analysis (see below) to obtain the total column density $N_{\rm CS}$ using Eq. G3. This assumption was only valid if our NH_3 and CS tracers probed the same gas. In all other cases, we assumed $T_{\rm kin}$=10 K.

In order to obtain the H_2 column density $N_{\rm H_2}$, we chose the abundance ratio $\chi_{\rm CS} = 4 \times 10^{-9}$ which was in the range of values $\chi_{\rm CS} = 10^{-9} \rightarrow 10^{-8}$ indicated by Irvine, Goldsmith & Hjalmarson (1987) who studied the chemical abundances inside several distinct regions e.g Orion KL and Sgr B2. Zinchenko et al. (1994) also chose this abundance ratio for the study of several CS cores. The derived H_2 parameters are scaled by the abundance ratio and thus may vary by a factor of two.

We provided total mass estimates by using the kinematic distance in Eq. G11 and considering the molecular gas consisted of 20% Helium. As per our CO analysis, we used a prolate geometry to provide H_2 density $n_{\rm H_2}$ estimates.

4.4 NH_3 analysis

To fit the emission of the NH_3(1,1) inversion transition, we used five Gaussians separated by known velocities to fit the main peak and the four satellite lines (Wilson, Bieging & Downes 1978). The fit parameters of each regions were listed in Table 3.

Whenever we detected NH_3(1,1) satellite lines, we used the ratio of the integrated intensity between the main and satellite line and used Eq. G4 to determine the averaged main line optical depth. Finally, based on the NH_3(1,1) partition function, we used Eq. G5 to estimate the optical depth of the NH_3(1,1) emission $\tau_{\rm NH_3(1,1)}$.

As per our CS analysis, we approximated our regions to be in LTE and used Eq. G7 to obtain the NH_3(1,1) column density. If NH_3(2,2) emission was also detected, we obtained the temperature $T_{\rm kin}$ using Eqs. G8 and G9. This method remains only valid for kinetic temperature below 40K. We then considered an even chemical abundance between ortho-NH_3 and para-NH_3 to obtain the total column density $N_{\rm NH_3}$ via Eq. G10. To convert the NH_3 column density into H_2 column density, we used an abundance ratio $\chi_{\rm NH_3} = 1 \times 10^{-8}$ which is in the range provided by Irvine, Goldsmith & Hjalmarson (1987). Finally, the same method as per our CS and CO analysis was used to determine the mass and density estimates. From Fig. 3, we find that the morphology of the gas detected by the NH_3(1,1) inversion transition coincides with the CS(1–0) emission towards the region covered by our 7mm survey.

4.5 HI analysis

In order to complete the picture of the gas distribution towards HESS J1826−130, we made use of SGPS data with $\Delta v = 0.8$ km/s and $T_{\rm rms}$=1.4 K/channel (McClure-Griffiths et al. 2005) to search for diffuse atomic gas.

Comparing HI and CO(1–0) is an effective method to provide kinematic distance ambiguity resolution of molecular clouds (KDAR, see Anderson & Bania 2009; Roman-Duval et al. 2010 for further details) provided we know the location of the continuum source appearing in the line of sight. For instance, Fig. 7 shows the association between the CO(1–0) emission (blue lines) and the HI absorption (black lines) in region *H1* and *H3*.

We also use the HI data to probe potential dips associated with energetic sources (e.g SNRs) in order to provide an estimate of their kinematic distance. Fig. 8 shows the HI integrated intensity towards HESS J1826−130 between $v_{\rm lsr} = 58 - 64$ km/s. We noticed a dip in HI emission towards SNR G018.6−0.2 which did not overlap with the ^{13}CO(1–0) contour shown in red. From the GRS ^{13}CO(1–0) longitude-velocity plot in Fig. E1, we also noted a lack of emission at $v_{\rm lsr} = 60 - 70$ km/s spatially coincident with this SNR position, with weak emission at $v_{\rm lsr} \sim 60$ km/s and ~ 75 km/s. These weak ^{13}CO(1–0) features may provide further evidence of a shell towards this SNR where molecular gas have been accelerated. Thus, we argue a shell has been produced by SNR G018.6−0.2's progenitor star located at $v_{\rm lsr} \sim 60 - 64$ km/s inferring a SNR distance $d = 4.5$ kpc (near) or 11.4 kpc (far).

4.6 Discussion of individual regions

4.6.1 Region R1

Region *R1* (RA=18.421h, Dec=−13.28°) is located 0.5° away from the pulsar PSR J1826-1334 and contains the bulk of the ^{13}CO(1–0) and CS(1–0) emission. From the CO(1-0) and ^{13}CO(1-0) molecular transitions, we detected four components with kinematic velocities $v_{\rm lsr} = 48$ km/s (*R1a*), $v_{\rm lsr} = 41$ km/s (*R1c*), $v_{\rm lsr} = 58$ km/s (*R1d*), and $v_{\rm lsr} = 67$ km/s (*R1e*). CS(1–0) was also found in *R1a,b,c*. However, only the component *R1a* and *R1b* remained visible in NH_3(1,1). The CS(1–0) emission in *R1a* ($v_{\rm lsr}$=48 km/s, see Table 2) is quite broad ($\Delta v_{\rm FWHM} \sim 10$ km/s) compared to the other fainter components along the line of sight.

We also found two 44GHz CH_3OH masers that we labeled *CH1* ($v_{\rm lsr}$ =46 km/s) and *CH2* ($v_{\rm lsr}$ =56 km/s) (see Fig. 6). They are thus associated to the molecular cloud traced by the component *R1a* and *R1d*. While the component *CH1* seems connected to the IR bubble *N22* (labeled by Churchwell et al. 2006), *CH2* is likely associated with the HII region HDRS G018.097-0.324 (*H2* in Fig. 6). We also found H51α, H62α, H65α, and H69α emission at $v_{\rm lsr} \sim 50 - 55$ km/s coincident with region *H1* at kinematic distances roughly agreeing with the distance

Table 2. Derived parameters of the Gaussian fits from the selected regions in Fig. 2 (see text). $v_{\rm cent}$ represents the velocity centroid of the Gaussian while Δv indicates the Gaussian FWHM. W=$\int T_{mb}{\rm d}v$ represents the integrated main beam intensity applying the main beam correction factor $\eta_{\rm mb}$ (see text for details). The components detected by the different tracers CS(1–0), ^{13}CO(1-0), CO(1-0) are labeled as 'a,b,c,d,e,f' according to their velocity range (see footnote below table).

CO(1–0)	R1 (RA,Dec)=(18.421h, −13.282°) Radii*=(405″ × 405″)				R2 (RA,Dec)=(18.420h, −13.125°) Radii=(135″ × 270″)			R3 (RA,Dec)=(18.429h, −13.178°) Radii=(64″ × 64″)		
	a	c	d	e	a	c	e	a	e	f
Peak value $T_{\rm A}^*$ (K)	13.6	4.5	2.7	4.9	11.0	4.3	8.0	6.2	7.0	10.0
$v_{\rm cent}$ (km/s)	49.6	41.2	57.8	66.2	52.0	41.8	67.9	46.0	70.5	33.1
Δv (km/s)	9.0	5.7	2.8	10.3	4.8	11.4	11.3	10.0	9.1	4.5
$W_{\rm CO}$ (K km/s)	148.2	31.0	7.2	60.0	64.4	59.2	108.3	75.6	76.6	53.6
$T_{\rm rms}$/ch/$\sqrt{\rm bins}$ (K)	—0.07—				—0.18—			—0.30—		
^{13}CO(1–0)	R1				R2			R3		
	a	c	d	e	a	c	e	a	e	f
Peak value $T_{\rm A}^*$ (K)	1.6	0.5	0.5	0.7	1.7	0.3	1.8	0.5	0.9	3.0
$v_{\rm cent}$ (km/s)	48.9	41.6	57.7	66.2	52.0	42.8	67.7	47.6	72.0	33.0
Δv (km/s)	7.5	2.8	2.8	5.6	2.8	13.9	7.1	3.9	3.9	3.4
$W_{^{13}{\rm CO}}$ (K km/s)	27.0	3.1	7.2	8.3	10.1	7.7	28.5	4.6	8.1	23.2
$T_{\rm rms}$/ch/$\sqrt{\rm bins}$ (K)	—0.01—				—0.01—			—0.03—		
CS(1–0)	R1				R2			R3		
	a	c	d	e	a	c	e	a	e	f
Peak value $T_{\rm A}^*$ (K)	0.2	< 0.1	-	0.1	0.2	-	0.4	-	0.1	0.9
$v_{\rm cent}$ (km/s)	49.7	41.9	-	66.2	51.8	-	67.9	-	70.8	33.1
Δv (km/s)	10.7	1.9	-	7.2	2.6	-	4.8	-	1.8	3.2
$W_{\rm CS}$ (K km/s)	4.7	0.2	-	1.3	1.4	-	5.3	-	0.7	7.5
$T_{\rm rms}$/ch/$\sqrt{\rm bins}$ (K)	—0.01—				—0.01—			—0.03—		

CO(1–0)	R4 (RA,Dec)=(18.422h, −12.832°) Radii=(175″ × 280″)			R5 (RA,Dec)=(18.449h, −13.336°) Radii=(150″ × 270″)			R6 (RA,Dec)=(18.385h, −14.049°) Radii=(460″ × 460″)
	a	b	e	a	b	d	b
Peak value $T_{\rm A}^*$ (K)	11.5	8.7	3.9	6.6	5.4	1.1	10.2
$v_{\rm cent}$ (km/s)	51.2	44.8	64.9	51.7	45.6	61.4	44.5
Δv (km/s)	4.6	4.9	5.6	5.4	6.5	7.9	6.3
$W_{\rm CO}$ (K km/s)	64.5	51.5	26.3	43.0	43.0	10.6	77.1
$T_{\rm rms}$/ch/$\sqrt{\rm bins}$ (K)	—0.23—			—0.24—			—0.10—
^{13}CO(1–0)	R4			R5			R6
	a	b	e	a	b	d	b
Peak value $T_{\rm A}^*$ (K)	1.8	1.6	0.4	0.3	1.0	-	1.3
$v_{\rm cent}$ (km/s)	51.3	45.1	65.0	52.0	46.7	-	44.4
Δv (km/s)	3.7	3.6	5.6	5.4	8.9	-4.8	
$W_{^{13}{\rm CO}}$ (K km/s)	15.3	13.0	4.7	3.5	19.2	-	13.6
$T_{\rm rms}$/ch/$\sqrt{\rm bins}$ (K)	—0.03—			—0.01—			—0.01—
CS(1–0)	R4			R5			R6
	a	b	e	a	b	d	b
Peak value $T_{\rm A}^*$ (K)	0.3	0.2	-	0.1	0.1	-	0.3
$v_{\rm cent}$ (km/s)	50.8	45.0	-	51.8	46.7	-	44.5
Δv (km/s)	2.6	2.8	-	2.2	4.7	-	4.0
$W_{\rm CS}$ (K km/s)	1.6	1.6	-	0.3	0.9	-	3.0
$T_{\rm rms}$/ch/$\sqrt{\rm bins}$ (K)	—0.01—			—0.01—			—0.01—

* Radii represents the dimensions of the ellipse (semi-minor axis × semi-major axis).
component a : $v_{\rm lsr} = 46 - 55$ km/s, matching the dispersion measure of P1.
component b : $v_{\rm lsr} = 44 - 46$ km/s.
component c : $v_{\rm lsr} = 39 - 44$ km/s.
component d : $v_{\rm lsr} = 55 - 62$ km/s.
component e : $v_{\rm lsr} = 62 - 75$ km/s.
component f : $v_{\rm lsr} = 30 - 35$ km/s.

Table 3. Derived parameters of the five Gaussian fits used to model $NH_3(1,1)$ emission, and the one Gaussian fit for the $NH_3(2,2)$ emission averaged over the region shown in Fig. 3. $T^*_{A_m}$ indicates the peak intensity of the main emission while $T^*_{A_s}$ are the peak intensities of the surrounding satellite lines. v_{cent} represents the velocity centroid of the Gaussian while Δv indicates the Gaussian FWHM. Finally W=$\int T_{mb} dv$ represents the integrated main beam intensity applying the main beam correction factor η_{mb} (see text for details). The different components detected by the different tracers CS(1-0), ^{13}CO(1-0), CO(1-0) are labeled as 'a,b,c,d,e,f' according to their velocity range (see footnote below table).

$NH_3(1,1)$	R1 (RA,Dec)=(18.419h, −13.284°) Radii=(395″ × 305″)				R2 (RA,Dec)=(18.420h, −13.125°) Radii=(135″ × 270″)			R3 (RA,Dec)=(18.429h, −13.178°) Radii=(64″ × 64″)		
	a	c	d	e	a	c	e	a	e	f
Peak value $T^*_{A_m}$ (K)	0.09	-	-	0.05	0.04	-	0.25	-	-	0.21
Peak value $T^*_{A_{s1}}$ (K)	0.03	-	-	-	-	-	0.13	-	-	0.05
Peak value $T^*_{A_{s2}}$ (K)	0.05	-	-	-	-	-	0.11	-	-	0.05
Peak value $T^*_{A_{s3}}$ (K)	0.02	-	-	-	-	-	0.11	-	-	0.08
Peak value $T^*_{A_{s4}}$ (K)	-	-	-	-	-	-	0.09	-	-	0.08
v_{cent} (km/s)	48.3	-	-	66.2	51.7	-	67.9	-	-	33.1
Δv (km/s)	6.4	-	-	4.5	1.8	-	4.5	-	-	2.7
$W_{NH_3(1,1)}$ (K km/s)	2.2	-	-	0.8	1.4	-	5.3	-	-	7.5
T_{rms}/ch/$\sqrt{bins}$ (K)	—0.01—				—0.01—			—0.01—		

$NH_3(2,2)$	R1				R2			R3		
	a	c	d	e	a	c	e	a	e	f
Peak value T^*_A (K)	0.03	-	-	-	-	-	0.10	-	-	0.13
v_{cent} (km/s)	51.5	-	-	-	-	-	67.9	-	-	33.1
Δv (km/s)	7.7	-	-	-	-	-	3.1	-	-	2.7
$W_{NH_3(2,2)}$ (K km/s)	0.5	-	-	-	-	-	0.6	-	-	0.7
T_{rms}/ch/$\sqrt{bins}$ (K)	—0.01—				—0.01—			—0.02—		

$NH_3(1,1)$	R4 (RA,Dec)=(18.422h, −12.832°) Radii=(175″ × 280″)			R5 (RA,Dec)=(18.449h, −13.336°) Radii=(150″ × 270″)			R6 (RA,Dec)=(18.385h, −14.049°) Radii=(460″ × 460″)
	a	b	e	a	b	d	b
Peak value $T^*_{A_m}$ (K)	0.08	0.08	-	0.06	-	-	-
Peak value $T^*_{A_{s1}}$ (K)	-	-	-	-	-	-	-
Peak value $T^*_{A_{s2}}$ (K)	-	-	-	-	-	-	-
Peak value $T^*_{A_{s3}}$ (K)	-	-	-	-	-	-	-
Peak value $T^*_{A_{s4}}$ (K)	-	-	-	-	-	-	-
v_{cent} (km/s)	45.1	51.6	-	46.5	-	-	-
Δv (km/s)	2.0	4.0	-	5.6	-	-	-
$W_{NH_3(1,1)}$ (K km/s)	0.3	0.6	-	0.7	-	-	-
T_{rms}/ch/$\sqrt{bins}$ (K)	—0.01—			—0.01—			—0.01—

$NH_3(2,2)$	R4			R5			R6
	a	b	c	a	b	c	
Peak value T^*_A (K)	-	-	-	-	-	-	-
v_{cent} (km/s)	-	-	-	-	-	-	-
Δv (km/s)	-	-	-	-	-	-	-
$W_{NH_3(2,2)}$ (K km/s)	-	-	-	-	-	-	-
T_{rms}/ch/$\sqrt{bins}$ (K)	—0.01—			—0.01—			—0.02—

* Radii represents the dimensions of the ellipse (semi-minor axis × semi-major axis).
component a : $v_{lsr} = 46 - 55$ km/s, matching the dispersion measure of P1.
component b : $v_{lsr} = 44 - 46$ km/s.
component c : $v_{lsr} = 39 - 44$ km/s.
component d : $v_{lsr} = 55 - 62$ km/s.
component e : $v_{lsr} = 62 - 75$ km/s.
component f : $v_{lsr} = 30 - 35$ km/s.

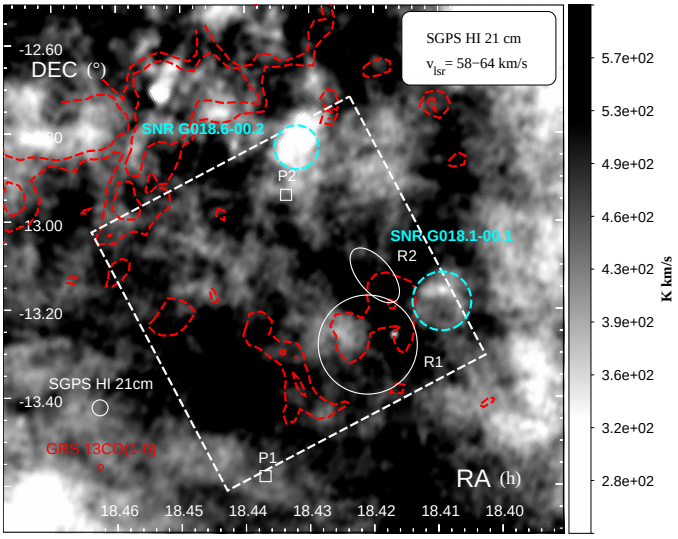

Figure 8. HI 21 cm integrated intensity in grey-scale between $v_{\rm lsr}$ = 58 − 64 km/s overlaid by the GRS ^{13}CO(1–0) contours in red (2.0 and 3.0 K km/s, see colour version). The white ellipses indicate the position of *R1* and *R2*, while cyan circles show the two SNRs. The white squares represent the pulsars PSR J1826−1334 (P1) and PSR J1826−1256 (P2). The white dashed box represent our Mopra 7mm coverage.

d=4.3 kpc proposed by Jackson (2004). From the HI 21 cm SGPS (McClure-Griffiths et al. 2005), we observed several absorptions features towards the region *H1* coincident with the CO(1–0) emission in *R1a* while no HI absorption was associated with *R1e*. (see Fig. 7). Consequently, the cloud is positioned in the near distance d=3.9 kpc.

Fig. 6 also shows the CS(1–0) and NH_3 integrated emission between $v_{\rm lsr}$ = 40 − 60 km/s and the recombination line H62α between $v_{\rm lsr}$ = 45 − 65 km/s.

We noted that the NH_3(1,1) appeared less prominent away from the region *H1*, *N21* and *N22* as opposed to the CS(1–0). Although the CS(1–0) emission appears uniform across *R1* between $v_{\rm lsr}$ = 40 − 60 km/s, the spectral lines averaged over the grid of boxes as shown in Fig. 9 reveals several contiguous cloud sub-components. For instance, the CS(1–0) emission indicated many line shape variations towards the south of *R1*, with several peaks with small velocity separations (e.g boxes 32 to 35), and rapid variations of the peak velocity (e.g boxes 13 to 17). Additionally, Fig. 4 also indicates that the NH_3(1,1) and CS(1−0) emission located at $v_{\rm lsr}$ = 45 − 60 km/s broad velocity structures to the CS and NH_3 compared to the emission in *R1e*.

The ^{13}CO(1–0) spectral lines illustrated similar features. Interestingly, from the three colour map in Fig. 9 showing the GRS ^{13}CO(1–0) integrated intensity between $v_{\rm lsr}$ = 45 − 50 km/s (red), $v_{\rm lsr}$ = 50 − 55 km/s (green), $v_{\rm lsr}$ = 55 − 60 km/s (blue), we observed that the structure shown in red was distinct from the arc-shaped structure displayed in green. We also noted a spatial overlap between all emission across the aforementioned velocity bands next to the HII region G018.15-0.29 which suggests there is a physical link between the HII region and the these structures. The presence of the double-peaked emission found in boxes 17 and 23 ($v_{\rm lsr}$=46 km/s and $v_{\rm lsr}$=56 km/s) which differs from the single-peaked emission found in box 5 ($v_{\rm lsr}$=51 km/s) may be caused by the presence of this continuum source. Consequently, it is likely that the component *R1a* and *R1d* are physically connected.

The physical parameters listed in Table H1.a in the appendix shows that the molecular gas traced by the *R1a* component is much more massive than the gas traced by the other components in the line of sight. From our CS and CO analysis, we found $M_{\rm H_2}$(CS)=1.0 × 10^{5}M$_\odot$ and $M_{\rm H_2}$ (CO) = 1.2 × 10^{5}M$_\odot$ respectively which is within the Virial mass range $M_{\rm vir}$ = 0.5 − 2.1 × 10^{5}M$_\odot$, and averaged densities $n_{\rm H_2}$(CS)=7.5 × 10^2 cm^{-3} and $n_{\rm H_2}$ (CO) = 9.6 × 10^2 cm^{-3}. The similar mass estimation from our CS and CO analysis may suggest the observed molecular gas are concentrated in clumps of density roughly equal to the CS(1–0) critical density $n_{\rm c}$ = 2 × 10^4 cm^{-3}. However, a lower mass and density estimates were attained with our NH_3 analysis with $M_{\rm H_2}$ = 1.4 × 10^{4}M$_\odot$ and $n_{\rm H_2}$ = 2.0 × 10^2 cm^{-3}.

4.6.2 Region R2

Towards region *R2* (RA=18.420h, Dec=−13.125°), we detected three CO(1–0) components with velocity $v_{\rm lsr}$ =51 km/s (*R2a*), $v_{\rm lsr}$ =43 km/s (*R2c*), $v_{\rm lsr}$ = 68 km/s (*R2e*) (see Table 2). However, ^{13}CO(1–0), CS(1–0) and NH_3(1,1) were solely found in *R2a* and *R2e*. We also observed $SiO_{v=0}$(1–0) emission, whose centroid velocity coincided with the component *R2e* revealing the presence of post-shocked gas (see Fig. 6). The combined detection of a 44GHz maser $CH_3OH(7_1–6_0)$ (region *CH3*), NH_3(3,3) (see Fig. B1) and cyanopolyyne HC_3N (region *HC3*, see Fig. F1) and their spatial connection with the IR source (see Fig. 6 left panel) suggested the shock may have been caused by outflows from nearby star forming regions.

Our CS and NH_3 analysis indicated that this molecular cloud was optically thick ($\tau_{\rm CS(1-0)}$=1.5 and $\tau_{\rm NH_3(1,1)}$=3.5). Consequently, the CO(1–0) emission may suffer strong optical depth effects which would cause line width broadening (Δv=12 km/s, see Table 2).

Assuming the molecular gas is located at d=4.6 kpc (near distance), we obtained the following masses $M_{\rm H_2}$ (CS) = 3.4 × 10^{4}M$_\odot$, $M_{\rm H_2}$ (NH_3) = 8.1 × 10^{4}M$_\odot$ and $M_{\rm H_2}$ (CO) = 2.9 × 10^{4}M$_\odot$ which were all within the Virial mass limits $M_{\rm vir}$ = 0.3 − 1.1 × 10^{5}M$_\odot$. We also determined the averaged densities $n_{\rm H_2}$ (NH_3) ∼ 4.8 × 10^3 cm^{-3},$n_{\rm H_2}$ (CS) ∼ 2.0×10^3 cm^{-3} and $n_{\rm H_2}$ (CO) ∼ 1.7 × 10^3 cm^{-3}.

The component *R2a* is associated to the component *R1a* (see Fig. 3) and the masses obtained are : $M_{\rm H_2}$ (CS) > 3.4 × 10^{3}M$_\odot$, $M_{\rm H_2}$ (NH_3) > 4.5 × 10^{2}M$_\odot$ and $M_{\rm H_2}$ (CO) = 1.3 × 10^{4}M$_\odot$, and densities $n_{\rm H_2}$ (CS) > 3.3 × 10^2 cm^{-3}, $n_{\rm H_2}$ (NH_3) > 4.3×10^1 cm^{-3} and $n_{\rm H_2}$ (CO) = 1.2 × 10^{3}cm^{-3} (see Table H1.b). The small fraction of dense gas detected by the CS and NH_3 tracers at $v_{\rm lsr}$ ∼ 50 km/s explains the large discrepancies between the different masses and densities.

Finally, our CO analysis revealed the H_2 mass traced by the component *R2c* is $M_{\rm H_2}$ = 8.8 × 10^{3}M$_\odot$ and a density $n_{\rm H_2}$ (CO) = 3.9 × 10^2 cm^{-3}.

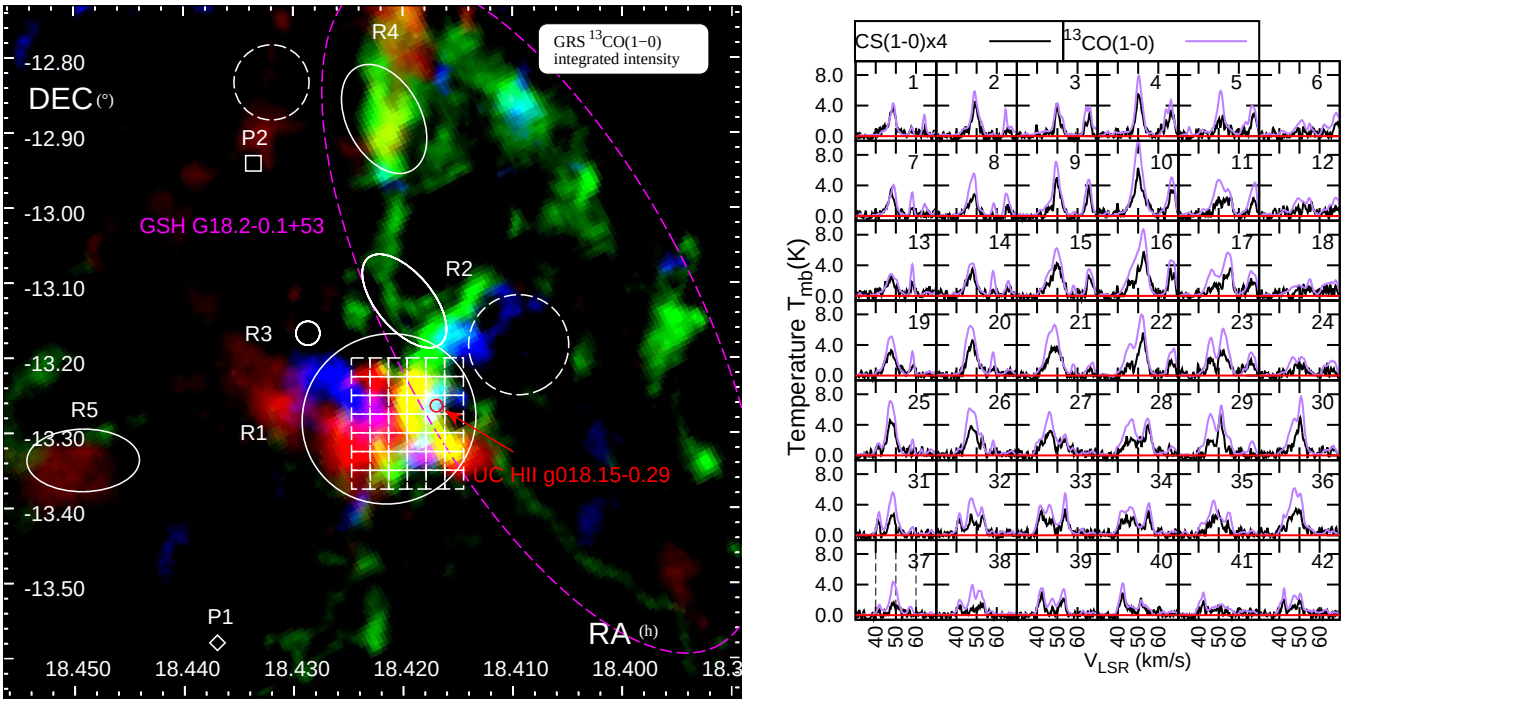

Figure 9. *(Left)* Three-colour image illustrating the GRS ^{13}CO(1–0) towards HESS J1826−130 integrated intensity at three velocity ranges : 45 − 50 km/s (red), 50 − 55 km/s (green), 55 − 60 km/s (blue). The HII region UC HII G018.15-0.29 is indicated in red. The purple dashed ellipse indicates the position and size of the putative molecular shell GSH 18.1-0.2+53 (Paron et al. 2013). *(Right)* Spectra of GRS ^{13}CO(1–0) (purple lines in colour version) and Mopra CS(1–0) emission (black lines) averaged over the boxes shown in the left panel.

4.6.3 Region R3

We detected three spectral components inside *R3* (RA,Dec)=(18.429h, −13.178°). The two components *R3a* and *R3e* from CO(1–0) and ^{13}CO(1–0) observations appear to be extensions of the molecular gas found in the regions *R1* and *R2*, and their masses listed in Table H1.c indicate small mass contribution. On the other hand, the component *R3f* ($v_{\rm lsr}$ = 43 km/s) showed prominent NH_3(1,1) and CS(1−0) emission. The additional detection of the cyanopolyyne HC_3N(5–4,F=4–3) suggested the molecular cloud may be associated with the HII regions G018.303-0.389 and G018.305-0.392 (White, Becker & Helfand 2005). From the HI spectral lines shown in Fig. 7, all CO(1–0) emission found in *R3* was associated with an HI absorption feature and consequently puts the molecular cloud in the far distance of d=13.4 kpc. Assuming the gas traced by the component *R3f* has an angular size equal to the Mopra NH_3(1,1) beam size, we obtained the following H_2 masses M_{H_2} (CS) = $1.5 \times 10^5 M_\odot$, M_{H_2} (NH_3) = $1.3 \times 10^4 M_\odot$, M_{H_2} (CO) = $1.5 \times 10^4 M_\odot$ and Virial mass $M_{\rm vir}$ = $0.7 - 2.5 \times 10^4 M_\odot$ which gives the following H_2 densities n_{H_2} (CS) = 7.6×10^3 cm^{-3}, n_{H_2} (NH_3) = 6.2×10^2 cm^{-3}, n_{H_2} (CO) = 9.3×10^2 cm^{-3}.

4.6.4 Region R4

Region *R4* located north of HESS J1826−130, is nearby the supernova remnant SNR G018.6−0.2. From NH_3(1,1) and CS(1–0) observations, we detected two components *R4a* and R4b with small velocity separation ($v_{\rm cent}$=45 km/s and $v_{\rm cent}$=51 km/s).

As shown in Fig. 4, we observed no CS and NH_3 emission connecting the components *R4a* and *R4b*. From Fig. 9, we noted that the molecular gas in *R4a* (shown in green) appeared to be part of the putative molecular shell GSH G018.2–0.1+53 suggested by Paron et al. (2013) whereas the gas in *R4b* (in red) appeared isolated. However, their similar morphologies as shown by the overlap of the two components (in yellow) the similarities of the ^{13}CO(1–0), CS, and NH_3 spectral lines may indicate some association.

Assuming *R4a* and *R4b* were situated at the near distance, we derived the total mass lower limit for *R4a* M_{H_2} (CS) > $7.4 \times 10^3 M_\odot$, M_{H_2} (NH_3) > $2.0 \times 10^3 M_\odot$, M_{H_2} (CO) = $1.6 \times 10^4 M_\odot$ and M_{H_2} (CS) > $5.0 \times 10^3 M_\odot$, M_{H_2} (NH_3) > $1.2 \times 10^3 M_\odot$ and M_{H_2} (CO) = $1.1 \times 10^4 M_\odot$ for *R4b* agreeing with their Virial mass ranges $M_{\rm vir} = 0.7 - 2.5 \times 10^4 M_\odot$ and $M_{\rm vir} = 0.6 - 2.2 \times 10^4 M_\odot$ respectively (see Table H1.d). From CO analysis, we obtained the densities n_{H_2} (CO) = 9.3×10^2cm^{-3} and n_{H_2} (CO) = 8.2×10^2 cm^{-3} for *R4a* and *R4b* respectively. In the case where *R4a* and *R4b* where associated to the same molecular complex at d∼4 kpc , the total mass obtained would be M_{H_2} (CO) ∼ $3.0 \times 10^4 M_\odot$.

Therefore, although the region *R4* is unlikely to be physically related to HESS J1825−137 and HESS J1826−130, it highlights the complexity of the structure of the molecular gas in the line of sight.

4.6.5 Region R5

The region *R5* is located 20′ away from the pulsar PSR J1826-1334. From CO(1–0) observations, three components in region *R5* with centroid velocity $v_{\rm cent}$=51 km/s (*R5a*), $v_{\rm cent}$=45 km/s (*R5b*), $v_{\rm cent}$=61 km/s (*R5d*) were detected. However, ^{13}CO(1–0), CS(1–0) were solely observed in *R5a* and *R5b* and weak NH_3(1,1) emission ($< 3T_{\rm rms}$) was found only in *R5a*.

From Fig. 4, it appears that most of the emission is located between $v_{\rm lsr} = 45$ km/s and $v_{\rm lsr} = 48$ km/s.

We derived H_2 masses of M_{H_2} (NH_3) $> 2.0 \times 10^3 M_\odot$, M_{H_2} (CS) $> 7.4 \times 10^2 M_\odot$, M_{H_2} (CO) $= 9.5 \times 10^3 M_\odot$ for *R5a* and M_{H_2} (CS) $> 1.8 \times 10^3 M_\odot$ and M_{H_2} (CO) $= 1.1 \times 10^4 M_\odot$ for *R5b*. Therefore, the molecular gas traced by *R5a* and *R5b* appears less clumpy as opposed to *R1a*. From CO(1–0) analysis, we obtained the densities n_{H_2} (CO) $= 6.8 \times 10^2$ cm^{-3} and n_{H_2} (CO) $= 6.1 \times 10^2$ cm^{-3} for *R5a* and *R5b* respectively (see Table H1.e). Therefore, the molecular clouds located inside *R5* are marginally denser than our other studied regions. If *R5a* and *R5b* were to be physically connected and located at d=4 kpc, we would obtain the following total mass M_{H_2} (CO) $= 2.3 \times 10^4 M_\odot$.

4.6.6 Region R6

The region *R6* is located in the southern part of HESS J1825-137. It is surrounded by several HII regions and the SNRs G017.4−0.1 and G017.0−0.0 We found CO and ^{13}CO(1-0) emission with a centroid velocity at $v_{\rm lsr} \sim 44$ km/s. As shown in Fig. 5, we noted that the CO(1–0) emission and its isotopologue ^{13}CO(1–0) revealed a broad positive wing ($v_{\rm lsr} = 45 - 55$ km/s). However our deep pointing in CS(1–0) revealed no such features.

From our deep pointing measurements, we obtained $N_{H_2} = 7.5 \times 10^{21}$ cm^{-2}. If we assumed the molecular clouds have uniform column density across the molecular clouds, we would obtain a total mass M_{H_2} (CS) $> 3.6 \times 10^4 M_\odot$(see Table H1.f), which would be a factor of two smaller than the mass derived using our Nanten CO(1–0) observations M_{H_2}(CO)=$7.6 \times 10^4 M_\odot$.

Region *R6* and the surrounding molecular gas reveals a broad spatial distribution of ^{13}CO(1–0) and the molecular cloud may be associated to the TeV source HESS J1825−137. This molecular cloud may therefore influence the morphology of the south region of the TeV PWN.

4.7 Summary

We detected several molecular clouds along the line of sight. Notably, we observed a small molecular cloud located at $v_{\rm lsr}$=18 km/s overlapping with the pulsar PSR J1826-1256 and whose kinematic distance d = 1.7 kpc roughly agreed with the pulsar's predicted distance d=1.4 kpc from Wang (2011).

The molecular gas located at $v_{\rm lsr} = 46 - 55$ km/s and matching the pulsar's distance have a mass M_{H_2}=$3.3 \times 10^5 M_\odot$ where $\sim$ 30% resides inside the region *R1*. Moreover, we observed prominent and extended CS(1–0) and NH_3(1,1) emission in *R1a* and thus it suggests that the observed molecular gas consists of dense clumps likely to exceed the CS(1–0) critical density $n_c \sim 2 \times 10^4$ cm^{-3} at 10 K.

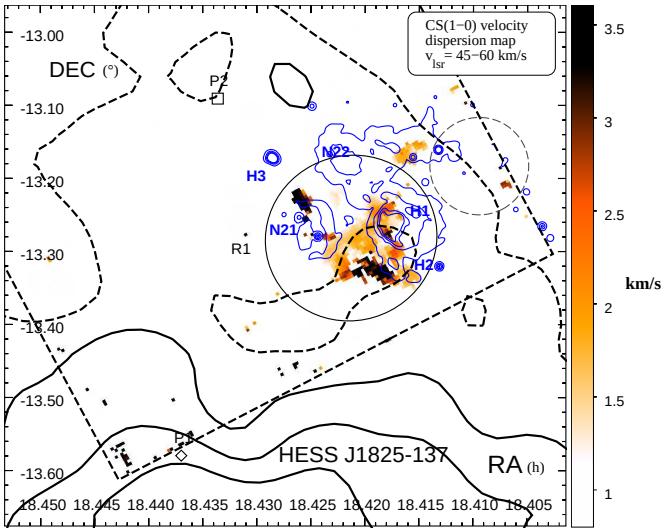

Figure 10. CS(1–0) velocity dispersion $v_{\rm disp}$ map between $v_{\rm lsr} = 45 - 60$ km/s with $T_A^* > 4T_{\rm rms}$, overlaid by the 8μm Spitzer GLIMPSE contours (blue in colour version).

The molecular gas traced by the component *R1a* also revealed complex CS and ^{13}CO(1–0) spectral lines surrounding the HII region G018.15-00.29 and towards HESS J1825−137 with several intensity peaks with little velocity separations and rapid variations of the velocity peaks.

We also remarked that the components found at $v_{\rm lsr} = 44 - 46$ km/s 'b' often overlapped and shared similar properties with the component 'a' at $v_{\rm lsr} = 46 - 55$ km/s which may indicate possible physical connection.

Finally the HI and ^{13}CO(1–0) data showed the presence of a plausible void centred at the SNR G018.6−0.2 at $v_{\rm lsr} \sim 60 - 65$ km/s and associated with the molecular cloud where the dense gas traced by the component *R2e* resided. This suggests that this SNR may be located at a distance d=4.6 kpc (near distance) or d=11.4 kpc (far distance).

5 DISCUSSION

5.1 Dynamics of the dense molecular gas in region *R1a*-Looking for the progenitor SNR

We focus now on the gas dynamics to probe the level of disruption in the observation of this region structure of CS(1–0). Bubbles, core-collapsing clouds and shocks are the common causes of gas disruption. We have shown that the dense molecular cloud traced by the component *R1a* displays complex morphology and spectral line profiles. The velocity dispersion, or second moment, map of CS(1–0) in Fig. 10 indicates broad dense gas overlapping with the HII region UC HII G018.15-0.28.

Most of the CS(1–0) emission towards the centre of *R1a* displays a mild velocity dispersion ($v_{\rm disp} \sim 2$ km/s). There is also no appreciably broad gas overlapping the IR bubbles *N21* and *N22*. However, we observe a $\sim 3.5-4$ km/s velocity dispersion to the south of *R1a* towards HESS J1825−137 which does not seem related to any IR emission as shown in Figs. 10.

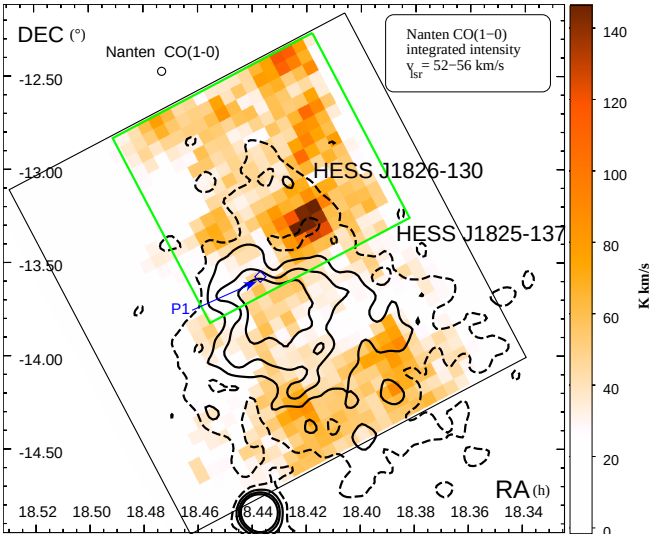

Figure 11. Nanten CO(1–0) integrated intensity between $v_{\rm lsr} = 52 - 56$ km/s overlaid by HESS TeV contours. The large black square represents the region where the overall averaged ambient density $n_{\rm amb}$ was estimated (see section 4.1) with the CO(1–0) emission within the green box (in colour version) being excluded.

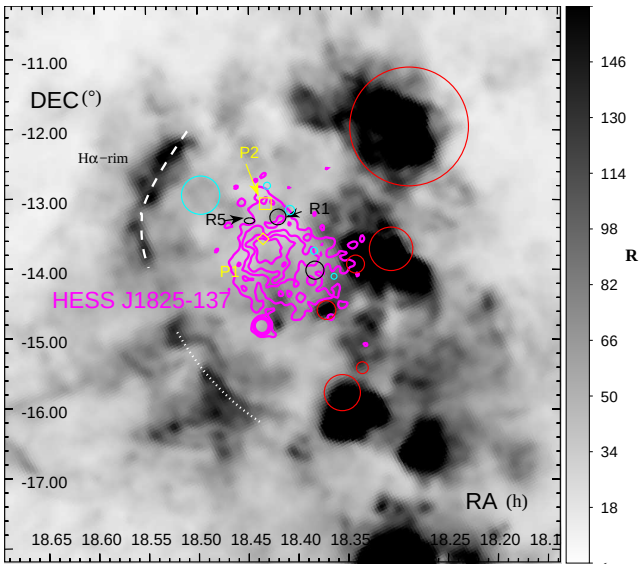

Figure 12. Hα image towards HESS J1825-137 in Rayleigh units overlaid by the HESS contours in magenta. The two pulsars labeled P1 and P2 are shown in yellow while the SNRs are displayed in cyan circles (see online version for colours). The white dashed lines represent the SNR Hα rim reported by Stupar, Parker & Filipović (2008) while the white dotted lines indicate another putative Hα rim which might be associated with the HESS J1825−137's progenitor SNR. The red circles encompassing the strong Hα emission on the right hand side are catalogued by Anderson et al. (2014) as HII regions.

We now focus on potential causes of the broad CS(1–0) lines in *R1a*. Little is known about the progenitor SNR of HESS J1825−137. From hydrodynamical simulation of the PWN, the radius of the SNR is expected to be four times the radius of this middle-aged PWN $r_{\rm SNR} \sim 4 r_{\rm PWN}$ (van der Swaluw et al. 2001). With the TeV radius of the PWN being $r_{\rm PWN} \sim 35$ pc (Aharonian et al. 2006), the predicted radius of the SNR thus becomes significantly large at $r_{\rm SNR} \sim 140$ pc.

de Jager & Djannati-Ataï (2009) indicated that the SNR's radius could reach $r_{\rm SNR} \sim 120$ pc if they assumed a kinetic energy $E_{\rm SN} = 3 \times 10^{51}$ erg from the supernova shock, an ambient density $n_{\rm amb} = 0.001$ cm^{-3}, and an age of the system $t_{\rm age} \sim 40$ kyr. By taking the Nanten CO(1–0) emission over a narrow $v_{\rm lsr}$ range (52−56 km/s) centred on the pulsar PSR J1826–1334 distance and discarding the contribution from the dense region inside the green box in Fig. 11, we obtain a density $n_{\rm H} \sim 4$ cm^{-3}. However, the typical noise level $T_{\rm rms}$/ch~ 0.4 K of the Nanten CO(1–0) data (Mizuno & Fukui 2004) greatly affects our density estimation which should then only be used as a upper-limit. Thus, our derived density does not at the moment refute the ambient density predicted by de Jager & Djannati-Ataï (2009). Besides this, due to the contamination of the CO(1–0) emission resulting from local and distant kinematic components, it also becomes difficult to identify the presence of the void caused by the SNR's progenitor star. The better sensitivity and velocity resolution of the NASCO (Fukui et al. 2006) or Nobeyama[4] surveys of the CO and ^{13}CO emission may provide solutions to this issue.

Interestingly though, Stupar, Parker & Filipović (2008) reported a Hα rim (see white dashed lines in Fig. 12) located roughly 120 pc away from PSR J1826-1334 (assuming the Hα rim is located at $d = 4$ kpc) and with a ratio SII/Hα ∼ 1.33 typical of SNR shock. Moreover, based on the sharp gradient in Hα, we might also speculate that the reported Hα rim is also seen to the south-east of HESS J1825−137 as shown in white dotted line in Fig. 12. The strong Hα emission to the west of HESS J1825−137 (red circles) has been catalogued as HII regions (Anderson et al. 2014). The projected separation of the Hα rim roughly matches with the SNR's expected radius based on $R_{\rm SNR}/R_{\rm PWN} \sim 4$ suggested by de Jager & Djannati-Ataï (2009). Furthermore, the lack of Hα emission north of HESS J1825−137 may arise due to the blocking effect of dense cloud responsible for the crushed PWN.

The possible association between the Hα rim and the TeV source could provide important information about the environment surrounding HESS J1825−137.

We now consider whether this SNR would contribute to the turbulence found inside *R1a*. We do not observe direct evidence of post-shocked gas inside at $v_{\rm lsr} = 45 - 60$ km/s such as SiO(1–0,v=0) emission or catalogued OH 1720 MHz masers. Nonetheless, if the shock did reach the cloud, we do expect the shock speed $v_{\rm s}$ to be considerably lowered due to the high averaged density found in this region. By applying Eq. 10 from Uchiyama et al. (2010) :

$$v_{\rm s} \approx 65 \left(\frac{n_{\rm R1a}}{100\ {\rm cm}^{-3}}\right)^{-1/2} \left(\frac{E_{\rm SN}}{10^{51}\ {\rm erg}}\right)^{1/2} \left(\frac{R_{\rm R1a}}{12.5\ {\rm pc}}\right)^{-3/2} {\rm km/s} \quad (1)$$

and assuming the distance to *R1a* boundary $R_{\rm R1a} = 20$ pc, a proton density found from our CO analysis $n_{\rm R1a} = 2.7 \times 10^3$ cm^{-3}, we find that the shock could reduce to a speed $v_{\rm s} \sim 10$ km/s. Consequently, using the age upper-limit $t = 40$ kyr for the SNR, the shock would

[4] http://www.nro.nao.ac.jp/ñro45mrt/html/index-e.html

have only travelled less than 1 pc (i.e an angular distance $\theta \sim 0.01^\circ$) inside the dense molecular cloud. Therefore, the SNR might only contribute to the disruptions found south of *R1a* (see Fig. 10) where we see a broader velocity dispersion $v_{\rm disp}$.

Alternatively, the broad velocity dispersion may also be caused by two distinct but contiguous velocity components as shown in Fig. 9 (red and green components) and thus may not be an indicator of randomly distributed disruption in this region. In fact, we note that this cloud shows similarities with the studied molecular clouds next to the Serpens cluster (Duarte-Cabral et al. 2011) and RCW120 (Torii et al. 2015), whose velocity components are thought to be caused by cloud-cloud collisions. Cloud-cloud collisions, studied using hydrodynamical simulations (Habe & Ohta 1992, Duarte-Cabral et al. 2011,Takahira, Tasker & Habe 2014,Torii et al. 2015), recently renewed popularity to explain the presence of high mass star-formation inside molecular clouds. Notably, such collisions between molecular clouds are thought to generate OB stars, filamentary clouds, dense cores and complex velocity distribution. In our region of study, Paron et al. (2013) in fact detected several O and B stars next to the IR bubble N22, N21 and the UC HII G018.15-00.28 towards the molecular gas *R1a* component.

5.2 TeV emission of HESS J1826–130

An important question is whether or not HESS J1826−130 can be associated with HESS J1825−137. Now, we will discuss potential origins of this northern TeV emission. For HESS J1826−130, Deil et al. (2015) reported its location at (18.434,−13.02°), and a TeV flux above 1 TeV $F(>1\ \mathrm{TeV}) = 7.4\times10^{-13}\,\mathrm{ph\,cm^{-2}\,s^{-1}}$.

5.2.1 CRs from the progenitor SNR of PSR J1826–1334

The general spatial match between the molecular cloud and the TeV emission of HESS J1826−130 may suggest a hadronic origin. Here, the progenitor SNR of HESS J1825−137 is an obvious candidate source for CRs in the region. A key question is whether the observed emission can be explained by the *sea* (Galactic plane averaged CR energy density $w_{\rm CR} \sim 1\,\mathrm{eV\,cm^{-3}}$) of cosmic-rays or require the presence of a nearby CR source. Using Eq. 10 from Aharonian (1991) and the mass of the molecular cloud $M_{\rm H_2} = 3.3\times10^5 \mathrm{M}_\odot$ calculated earlier, we obtain $F(>1\ \mathrm{TeV}) = 5.8\times10^{-14}\,\mathrm{ph\,cm^{-2}\,s^{-1}}$ produced by the sea of cosmic-rays towards HESS J1826−130. This predicted flux is ∼15 times below the observed flux estimated above. Therefore a nearby accelerator providing CRs at an energy density 15 times the Earth-like value is required. The required CR density enhancement to produce the observed TeV flux towards HESS J1826−130 can easily be reached by SNRs (e.g W28; see Aharonian et al. 2008). Therefore, the progenitor SNR of PSR J1826−1334 may contribute to the HESS J1826−130 TeV emission.

5.2.2 Other potential particle accelerators

Paron et al. (2013) argued the distance of SNR G018.2−0.1 to be $d = 4$ kpc based on its possible association with the nearby HII regions. Its small projected radius $r \sim$4 pc would imply a very young SNR with age < 1000 yr. By comparing our CO(1–0) column density the those derived from X-ray measurements $N_{\rm H} = 7.2\times10^{22}\,\mathrm{cm^{-2}}$ (Sugizaki et al. 2001) and $N_{\rm H} = 5.7\times10^{22}\,\mathrm{cm^{-2}}$ (Leahy, Green & Tian 2014), we would argue an SNR distance greater than 4 kpc, consistent with the distance estimate from Leahy, Green & Tian (2014). Additionally, Pavlovic et al. (2014) suggest a much further distance $d > 8.8$ kpc based on their updated $\Sigma - D$ relation. In the case where the SNR is located at $d = 4$ kpc, CRs would probably remain confined inside the SNR shock and would not be responsible of the TeV γ-ray emission found in HESS J1826−130. We did not find molecular gas overlapping the HESS J1826−130 emission in the case where $d > 4$ kpc. Therefore, we suggest that the TeV γ-ray emission towards HESS J1826−130 cannot be produced by CRs accelerated by the SNR G018.2−0.1.

The radio-quiet pulsar PSR J1826−1256 (P2), which powers the diffuse X-ray nebula PWN G018.5−0.4 (Roberts, Romani & Kawai 2001; Roberts et al. 2007), may also be a candidate for the origin of HESS J1826−130. The distance $d = 1.2 - 1.4$ kpc suggested by Wang (2011) infers a TeV γ-ray efficiency $\eta_\gamma \sim 2\times10^{-4}$ which is at the lower end of typical η_γ values for $\dot{E}_{\rm SD} \sim 10^{36-37}\,\mathrm{erg\,s^{-1}}$ (Kargaltsev, Rangelov & Pavlov 2013). We find that the Nanten CO(1–0) emission located at this distance ($v_{\rm lsr} = 10 - 25$ km/s, see Fig. D1) overlaps the pulsar and makes the PWN scenario at this distance unlikely. However, the adjacent position of the molecular gas at $v_{\rm lsr} = 60 - 80$ km/s (with near/far distance $d = 4.6/11.4$ kpc) appears spatially consistent with the PWN scenario. The molecular cloud north of P2 indeed support the offset position of the pulsar (coincident with AX J1826.1−1257, see Ray et al. 2011) with respect to the X-ray (Roberts et al. 2007) and TeV emission. At these distances, η_γ would then rise to 1.5×10^{-3} ($d = 4.6$ kpc) and 1.0×10^{-2} ($d = 11.4$ kpc), more consistent with the canonical η_γ values.

The plausible shell at $v_{\rm lsr} = 60 - 65$ km/s spatially coincident with the SNR G018.6−0.4 puts this SNR at the same distance to the pulsar P2 and may suggest an association between the two objects. To reconcile the small size of SNR G018.6−0.2 and the characteristic age of P2 ($\tau_c = 13$ kyr), they need to be placed at a far distance ∼ 11.4 kpc. Finally, the lack of an overlap in the 60−80 km/s gas and HESS J1826−130 would tend to rule out any direct association with SNR G018.6−0.2.

6 CONCLUSIONS

In this paper, we presented a detailed picture of the ISM surrounding HESS J1825−137, powered by the pulsar PSR J1826–1334 (here labelled P1) and discussed morphological and spectral properties of the TeV source.

Following Lemiere, Terrier & Djannati-Ataï (2006)'s detection of a molecular cloud overlapping HESS J1826−130, we carried out a study of the diffuse and the dense molecular gas across the region using the Nanten CO(1–0) Galactic

survey, the GRS ^{13}CO(1–0) data, and our 7mm and 12mm Mopra observations tracing CS(1–0) and NH_3(1,1).

We observed that the bulk of the molecular gas towards HESS J1826−130 was located at $v_{\rm lsr} = 45 - 60\,$km/s which appeared consistent with the dispersion measure distance of P1. We also noted a dense region at (RA, Dec)=(18.421h, −13.282°) with mass $M_{\rm H_2} \sim 1 \times 10^5 {\rm M}_\odot$ and H_2 density $n_{\rm H_2} \sim 7 \times 10^2\,{\rm cm}^{-3}$ which showed enhanced turbulence. We indicated that its CS(1–0) and ^{13}CO(1–0) velocity structure, the presence of a UC HII region and several OB stars and high mass star-forming regions, can be signatures of turbulent clouds caused by cloud cloud collisions (e.g RCW 120 Torii et al. 2015). We also suggested that its possible interaction with P1's progenitor SNR was unlikely to cause such disruptions.

The Hα rim discovered by Stupar, Parker & Filipović (2008) may be associated with P1's progenitor SNR, as the distance between the Hα rim and P1 appears consistent with an SNR radius $R_{\rm SNR} \sim 120\,$pc suggested by de Jager & Djannati-Ataï (2009) based on their suggestion that radius of the SNR being ~ 4 times that of the corresponding PWN.

We found that CRs produced by the P1's progenitor SNR could explain to the TeV γ-ray emission found in HESS J1826−130. The origin of HESS J1826−130 might also be leptonic. if associated with the PWN G018.5−0.4. If this PWN produces the HESS J1826−130 emission, the adjacent molecular gas at $v_{\rm lsr} = 60 - 80\,$km/s may explain the TeV morphology and would suggest a PWN distance $d = 4.6\,$kpc (near) or $d = 11.4\,$kpc (far). SNR G018.2−0.1 and SNR G018.6−0.2 (see Brogan et al. 2006 and Green 2014) are also positioned close to HESS J1826−130. Their small angular diameters however and their offset position makes the two SNRs unlikely to be associated with HESS J1826−130.

Further VHE observations with H.E.S.S would provide more refined spatial resolution with advanced analysis (e.g Parsons & Hinton 2014). This will enable a detail comparison between the TeV emission and the molecular gas and consequently add key information about the hadronic and/or leptonic nature of HESS J1826−130, and probe the diffusion of CRs into the gas (e.g see Gabici, Aharonian & Blasi 2007).

ACKNOWLEDGMENTS

The Mopra radio telescope is part of the Australia Telescope National Facility which is funded by the Australian Government for operation as a National Facility managed by CSIRO. Operations support was provided by the University of New South Wales and the University of Adelaide. The University of New South Wales Digital Filter Bank used for the observations with the Mopra Telescope (the UNSWMOPS) was provided with support from the Australian Research Council (ARC). This research has made use of the SIMBAD database, operated at CDS, Strasbourg, France.

REFERENCES

Aharonian F. et al., 2008, A&A, 481, 401
Aharonian F. et al., 2006, A&A, 460, 365
Aharonian F. A., 1991, Ap&SS, 180, 305
Anderson L. D., Bania T. M., 2009, ApJ, 690, 706
Anderson L. D., Bania T. M., Balser D. S., Cunningham V., Wenger T. V., Johnstone B. M., Armentrout W. P., 2014, ApJS, 212, 1
Anderson L. D., Bania T. M., Balser D. S., Rood R. T., 2011, ApJS, 194, 32
Blondin J. M., Chevalier R. A., Frierson D. M., 2001, ApJ, 563, 806
Brogan C. L., Gelfand J. D., Gaensler B. M., Kassim N. E., Lazio T. J. W., 2006, ApJ, 639, L25
Churchwell E. et al., 2009, PASP, 121, 213
Churchwell E. et al., 2006, ApJ, 649, 759
Dame T. M., Hartmann D., Thaddeus P., 2001, ApJ, 547, 792
de Jager O. C., Djannati-Ataï A., 2009, in Astrophysics and Space Science Library, Becker W., ed., Vol. 357, p. 451
Deil C., Brun F., Carrigan S., Chaves R., Donath A., Gast H., Marandon V., Terrier R., 2015, in 34th International Cosmic Ray Conference (ICRC 2015), PoS, announcement of new H.E.S.S galactic plane sources.
Duarte-Cabral A., Dobbs C. L., Peretto N., Fuller G. A., 2011, A&A, 528, A50
Frerking M. A., Wilson R. W., Linke R. A., Wannier P. G., 1980, ApJ, 240, 65
Fukui Y. et al., 2006, Proc. IAU Symp. 1, Astronomical Facilities of the Next Decade, 1, 21
Gabici S., Aharonian F. A., Blasi P., 2007, Ap&SS, 309, 365
Green D. A., 2014, Bull. Astron. Soc. India, 42, 47
Gusdorf A., Cabrit S., Flower D. R., Pineau Des Forêts G., 2008, A&A, 482, 809
Habe A., Ohta K., 1992, PASJ, 44, 203
Ho P. T. P., Townes C. H., 1983, ARA&A, 21, 239
Irvine W. M., Goldsmith P. F., Hjalmarson A., 1987, in Astrophysics and Space Science Library, Vol. 134, Interstellar Processes, Hollenbach D. J., Thronson Jr. H. A., eds., p. 561
Jackson J. M., 2004, in ASP Conf. Ser., Vol. 322, The Formation and Evolution of Massive Young Star Clusters, Lamers H. J. G. L. M., Smith L. J., Nota A., eds., p. 227
Kargaltsev O., Rangelov B., Pavlov G., 2013, Pulsar-Wind Nebulae as a Dominant Population of Galactic VHE Sources, pp. 359–406
Leahy D., Green K., Tian W., 2014, MNRAS, 438, 1813
Lemiere A., Terrier R., Djannati-Ataï A., 2006, Astrophysics, preprint (ArXiv : e-prints)
McClure-Griffiths N. M., Dickey J. M., Gaensler B. M., Green A. J., Haverkorn M., Strasser S., 2005, ApJS, 158, 178
Mizuno A., Fukui Y., 2004, in ASP Cong. Ser., Vol. 317, Milky Way Surveys: The Structure and Evolution of our Galaxy. Astron. Soc. Pac., San Francisco, Clemens D., Shah R., Brainerd T., eds., p. 59
Morris M., Turner B. E., Palmer P., Zuckerman B., 1976, ApJ, 205, 82
Paron S., Weidmann W., Ortega M. E., Albacete Colombo J. F., Pichel A., 2013, MNRAS, 433, 1619
Parsons R. D., Hinton J. A., 2014, Astropart. Phys., 56, 26
Pavlovic M. Z., Dobardzic A., Vukotic B., Urosevic D.,

2014, Serb. Astron. J., 189, 25
Protheroe R. J., Ott J., Ekers R. D., Jones D. I., Crocker R. M., 2008, MNRAS, 390, 683
Ray P. S. et al., 2011, ApJS, 194, 17
Roberts M. S. E., Gotthelf E. V., Halpern J. P., Brogan C. L., Ransom S. M., 2007, in WE-Heraeus Seminar on Neutron Stars and Pulsars 40 years after the Discovery, Becker W., Huang H. H., eds., p. 24
Roberts M. S. E., Romani R. W., Kawai N., 2001, ApJS, 133, 451
Roman-Duval J., Jackson J. M., Heyer M., Rathborne J., Simon R., 2010, ApJ, 723, 492
Schilke P., Walmsley C. M., Pineau des Forets G., Flower D. R., 1997, A&A, 321, 293
Strong A. W., Moskalenko I. V., Reimer O., Digel S., Diehl R., 2004, A&A, 422, L47
Stupar M., Parker Q. A., Filipović M. D., 2008, MNRAS, 390, 1037
Sugizaki M., Mitsuda K., Kaneda H., Matsuzaki K., Yamauchi S., Koyama K., 2001, ApJS, 134, 77
Takahira K., Tasker E. J., Habe A., 2014, ApJ, 792, 63
Torii K. et al., 2015, ApJ, 806, 7
Uchiyama Y., Blandford R. D., Funk S., Tajima H., Tanaka T., 2010, ApJ, 723, L122
Urquhart J. S. et al., 2010, PASA, 27, 321
van der Swaluw E., Achterberg A., Gallant Y. A., Tóth G., 2001, A&A, 380, 309
Voronkov M. A., Caswell J. L., Ellingsen S. P., Green J. A., Breen S. L., 2014, MNRAS, 439, 2584
Walsh A. J. et al., 2011, MNRAS, 416, 1764
Wang W., 2011, Res. Astron. Astrophys., 11, 824
White R. L., Becker R. H., Helfand D. J., 2005, AJ, 130, 586
Wilson T. L., Bieging J., Downes D., 1978, A&A, 63, 1
Zinchenko I., Forsstroem V., Lapinov A., Mattila K., 1994, A&A, 288, 601

APPENDIX A: BEAM EFFICIENCY AND COUPLING FACTOR

The Mopra main beam only receives only a fraction of the true emission, the rest being taken by the side lobes. Urquhart et al. (2010) obtained the main beam efficiencies, $\eta_{\rm mb}$, at different frequencies by calibrating the Antenna flux while observing Jupiter. The following coefficient will be useful to get the real antenna temperature of the source:

$$T_{mb} = \frac{T_A^*}{\eta_{mb}} \quad \text{(A1)}$$

The coupling factor fK brings the true brightness temperature for core sizes smaller than the beam size. Indeed, the beam will average the signal from the core with the noise coming from the rest of the beam, minimizing its strength.

$$fK = \left(1 - \exp\left(-\frac{4R^2}{\theta_{mb}^2} ln2\right)\right)^{-1} \quad \text{(A2)}$$

$$\frac{\Delta\Omega_{\rm A}}{\Delta\Omega_{\rm S}} = \frac{1}{fK} \quad \text{(A3)}$$

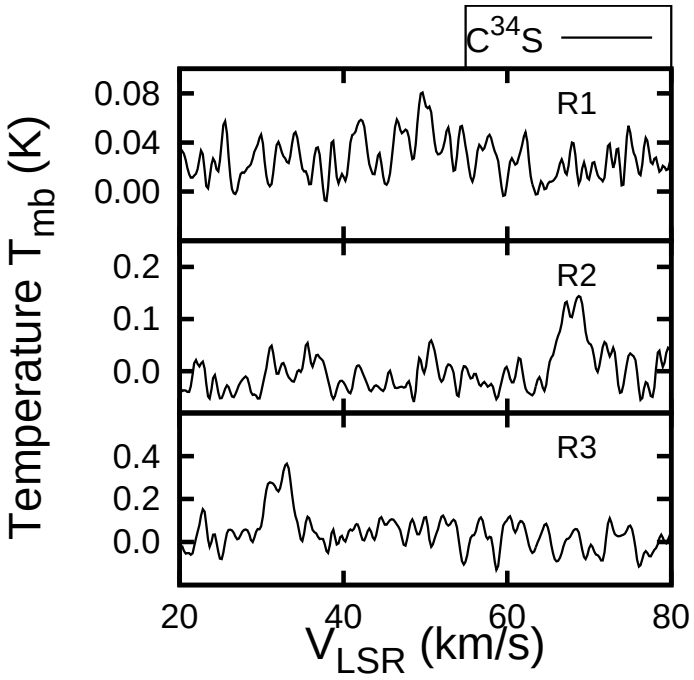

Figure C1. Averaged $C^{34}S$(1-0) emission over the 3 regions of interest *R1, R2, R3*.

APPENDIX B: NH3(2,2) AND NH_3(3,3)

Fig. B1 presents the NH_3(2,2) and NH_3(3,3) integrated intensities map for emissions located in the different kinematic velocity spans: $20-40$ km/s, $40-60$ km/s and $60-80$ km/s. It appears that R1, R2 and R3 shows significant emission of NH_3(2,2). However NH_3(3,3) are mostly found inside *R2* and *R3*.

APPENDIX C: $C^{34}S$(1-0)

Fig. C1 displays the averaged $C^{34}S$(1-0) emission profiles found in *R1, R2* and *R3*.

APPENDIX D: CO(1–0) EMISSION AT $V_{\rm LSR} = 10 - 25$ KM/S

Fig. D1 shows the Nanten CO(1–0) integrated intensity between $v_{\rm lsr}$ =10-25 km/s matching the pulsar PSR J1826-1256 (P2) kinematic distance. The presence of a molecular cloud (red circle) spatially overlapping the pulsar is observed. Provided the TeV emission originated from the PWN powered by P2, the association with the molecular cloud would have significantly affected the morphology of the TeV emission.

APPENDIX E: ^{13}CO(1–0) EMISSION POSITION-VELOCITY PLOTS TOWARDS SNR G018.6−0.2

Fig. E1 shows the ^{13}CO(1–0) position-velocity (in galactic coordinates) map towards the SNR G018.6−0.2. We observe from the Galactic longitude-velocity plot a drop of 13CO at $v_{\rm lsr} = 60-70$ km/s towards the SNR (whose boundaries are

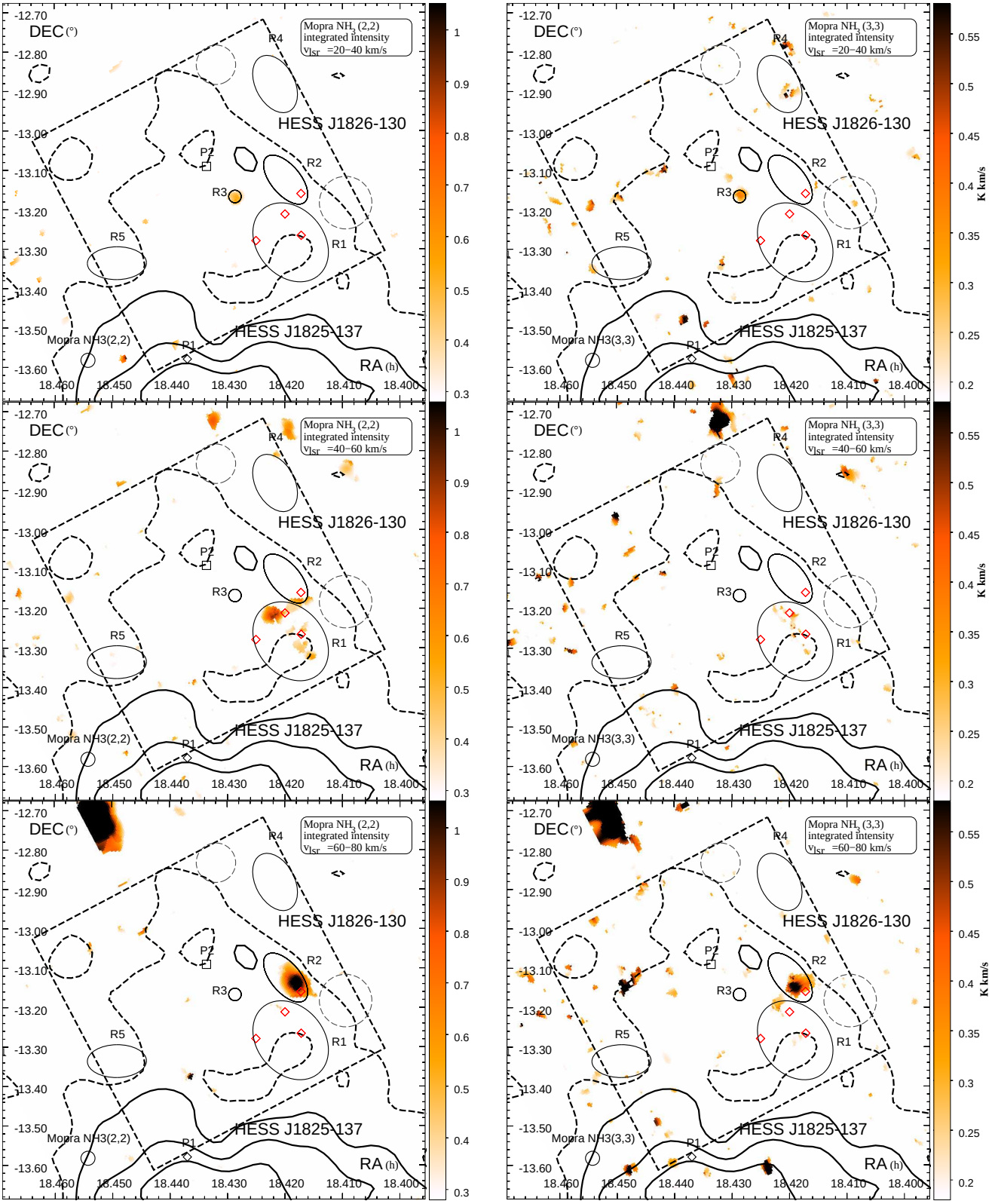

Figure B1. $NH_3(2,2)$ and $NH_3(3,3)$ integrated velocity over the different kinematic velocity spans : $v_{\rm lsr} = 20 - 40\,{\rm km/s}$, $v_{\rm lsr} = 40 - 60\,{\rm km/s}$, $v_{\rm lsr} = 60 - 80\,{\rm km/s}$. The diamonds represent the different HII regions next to *R1*. The black circles represent the size of the catalogued SNRs. The region covered by our 7mm survey is shown as a black dashed rectangle.

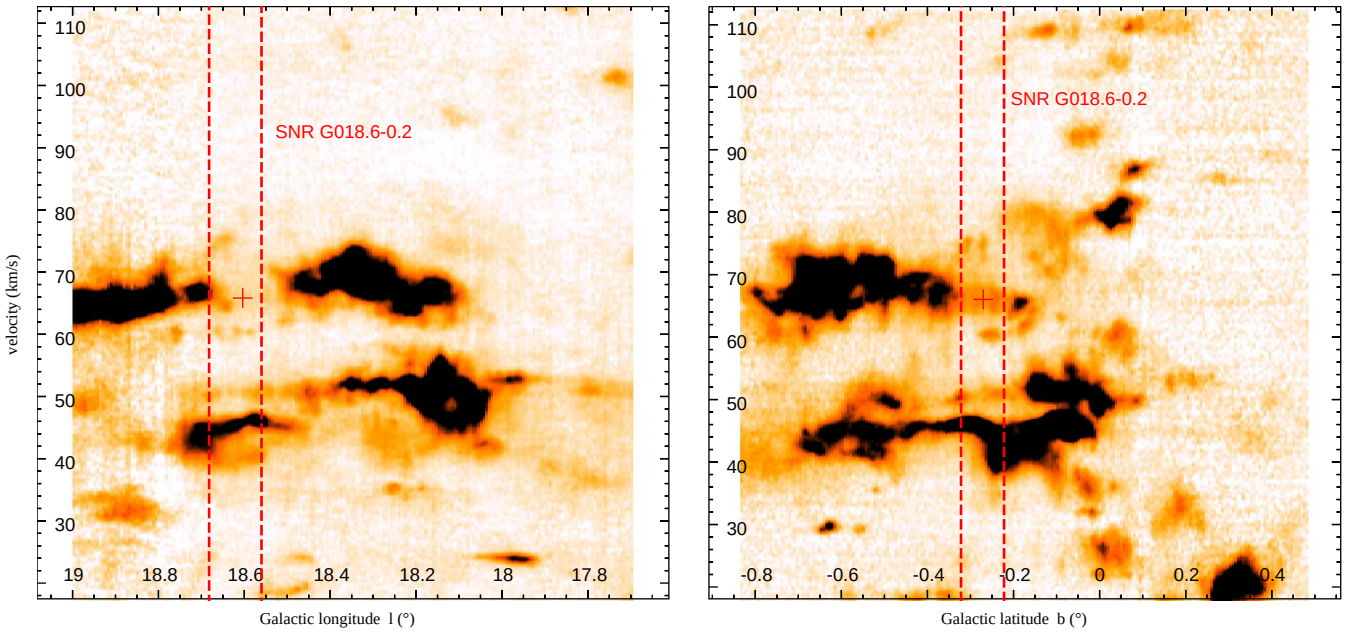

Figure E1. GRS ^{13}CO(1–0) Galactic longitude-velocity (l,v) *(left)* and Galactic latitude-velocity (b,v) *(right)* maps integrated between $b = [-0.227 : -0.338]$ and $l = [18.554 : 18.687]$. The red cross indicates the plausible location of a weak shell spatially coincident with the SNR G018.6−0.2 whose position is delimited by the two red dashed lines (see online version for colours).

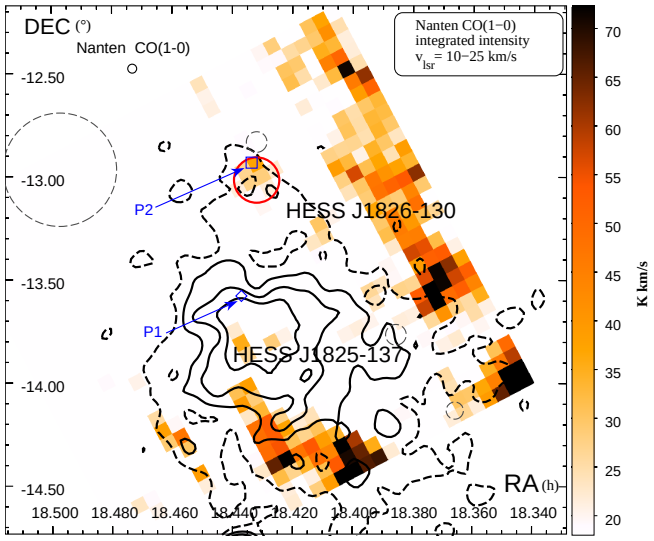

Figure D1. Nanten CO(1–0) integrated intensity between $v_{\rm lsr} = 10-25$ km/s overlaid by the HESS TeV contours in black (dashed and solid). The pulsars are displayed in blue while the SNRs are represented in grey dashed circles. The red circle highlights the molecular gas close to the pulsar PSR J1826–1256 (P2) highlighted in the text. The black dashed rectangle represents the region covered by our 7mm survey (see online version).

shown as red dashed lines). However, weak emission appears at $v_{\rm lsr} \sim 60$ km/s and 75 km/s (appearing in both maps) suggesting that gas may have been accelerated. Its spatial coincidence with the SNR position support the scenario of a putative shell produced by the SNR progenitor star.

APPENDIX F: HC_3N(5-4,F=4-3)

Fig. F1 shows the position of the observed HC_3N(5-4,F=4-3) position, and their respective spectra.

APPENDIX G: PHYSICAL PARAMETERS DERIVATION

G1 CS parameters

CS(1–0) optical depth:

$$\frac{W_{CS(1-0)}}{W_{C^{34}S(1-0)}} = \frac{1-e^{-\tau_{CS(1-0)}}}{1-e^{\alpha\tau_{CS}(1-0)}} \qquad \text{(G1)}$$

where α represents the relative abundance ratio $C^{34}S$/CS=0.04 (see section 4).

Column density of energy state 1 :

$$N_{CS_1} = \frac{8k\pi\nu_{10}^2}{A_{10}hc^3}\left(\frac{\Delta\Omega_{\rm A}}{\Delta\Omega_{\rm S}}\right)\left(\frac{\tau_{\rm CS(1-0)}}{1-e^{-\tau_{\rm CS(1-0)}}}\right)\int T_{\rm mb}\,(v)\,dv \qquad \text{(G2)}$$

where ν_{10} and A_{10} is the rest frequency and Einstein's coefficient of the CS(1–0) emission respectively. $\Delta\Omega_{\rm A}$ and $\Delta\Omega_{\rm S}$ are the antenna and source solid angle respectively. In the case where $\Delta\Omega_{\rm A} > \Delta\Omega_{\rm S}$, we use Eqs. A2 and A3.

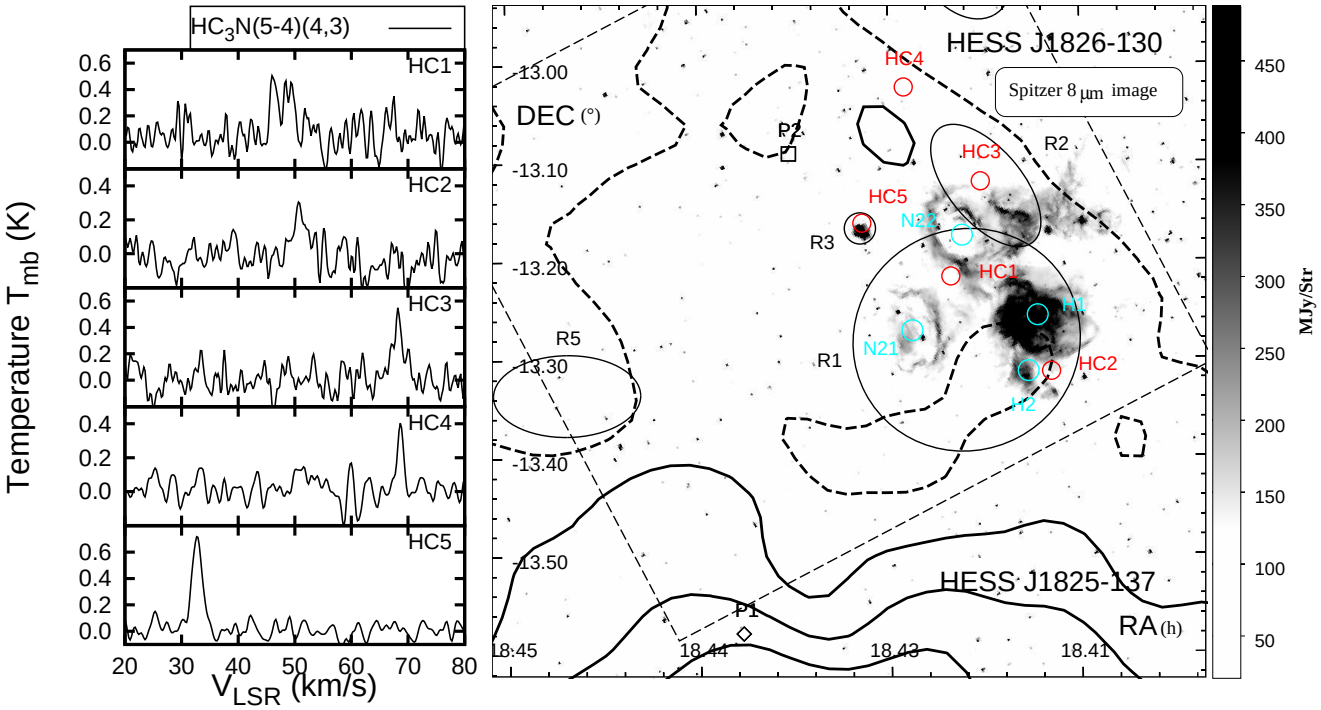

Figure F1. Spitzer 8μm map towards HESS J1826−130. The red circles indicate the regions where HC_3N(5–4,F=4–3) emission are found. Their respective spectra are shown in the left hand side. The aforementioned HII regions are displayed as cyan circles (see online version for colours).

CS column density :

$$N_{CS} = N_{CS_1}\left(1+\frac{1}{3}e^{2.35/T_{\rm kin}}+\frac{5}{3}e^{-4.7/T_{\rm kin}}+...\right) \quad \text{(G3)}$$

G2 NH_3 parameters

NH_3(1,1) optical depth :

$$\frac{T^*_{\rm A_m}}{T^*_{\rm A_s}} = \frac{1-e^{-\tau_{\rm m}}}{1-e^{\alpha\tau_{\rm m}}} \text{ for NH}_3 \quad \text{(G4)}$$

$$\tau_{\rm NH_3(1,1)} = \frac{\tau_{\rm m}}{0.5} \quad \text{(G5)}$$

Now, $\tau_{\rm m}$ is the optical depth of the main emission and α represents the relative strength of the satellite line compared to the main line.

NH_3(1,1) and NH_3(2,2) column densities :

$$N_{1,1} = \frac{8k\pi\nu_{11}^2}{A_{11}hc^3}\left(\frac{\Delta\Omega_{\rm A}}{\Delta\Omega_{\rm S}}\right)\left(\frac{\tau_{\rm NH_3(1,1)}}{1-e^{-\tau_{\rm NH_3(1,1)}}}\right)\int T_{\rm mb}\,(v)\,dv \quad \text{(G6)}$$

$$N_{2,2} = \frac{8k\pi\nu_{22}^2}{A_{22}hc^3}\left(\frac{\Delta\Omega_{\rm A}}{\Delta\Omega_{\rm S}}\right)\left(\frac{\tau_{\rm NH_3(2,2)}}{1-e^{-\tau_{\rm NH_3(2,2)}}}\right)\int T_{\rm mb}\,(v)\,dv \quad \text{(G7)}$$

where ν_{11} and ν_{22} are the rest frequencies of the NH_3(1,1) and NH_3(2,2) emission respectively. $\Delta\Omega_{\rm A}$ and $\Delta\Omega_{\rm S}$ are the antenna and source solid angle respectively. In the case where $\Delta\Omega_{\rm A} > \Delta\Omega_{\rm S}$, we use Eqs. A2 and A3.

Rotational and kinetic temperature

$$T_{\rm rot} = -\frac{41}{ln\,(3N_{2,2}/\,(5N_{1,1}))} \quad \text{(G8)}$$

$$T_{\rm kin} = T_{\rm rot}\left(1-\frac{T_{\rm rot}}{42}\log\left(1+1.1\exp\left(-16/T_{\rm rot}\right)\right)\right)^{-1} \quad \text{(G9)}$$

NH_3 column density

$$N_{tot} = N_{1,1}\left(1+\frac{1}{3}e^{23.26/T_{\rm kin}}+\frac{14}{3}e^{-100.25/T_{\rm kin}}+...\right) \quad \text{(G10)}$$

G3 Mass and density

$$M_{\rm H_2}\,(X) = \mu m_{\rm H}\pi ab N_{\rm H_2} \quad \text{(G11)}$$

$$n_{\rm H_2}\,(X) = \frac{M}{4/3\,(\mu m_{\rm H})\,\pi ab^2} \quad \text{(G12)}$$

where $\mu = 2.8$ represents the weight factor assuming the molecular cloud consisted of 20% of He, X was either NH_3 or CS and a, b was the semi-minor and semi-major axis respectively. ab^2 assumes the cloud also extends at distance b in the z-direction.

APPENDIX H: GAS PARAMETERS DERIVED FOR REGIONS *R1* TO *R6*

Table H1a. Parameters derived towards region *R1* using the molecular transition CS(1-0), CO(1-0), ^{13}CO(1-0), NH_3(1,1), NH_3(2,2) and $C^{34}S$(1-0) when emission are found. The labels *a,b,c,d* denote a distinct emission. Lower limits have been derived when we assumed $\tau = 0$

CS	R1	distance (kpc)	$\frac{W_{CS(1-0)}}{W_{C^{34}S(1-0)}}$	$\tau_{CS(1-0)}$	N_{CS} $[10^{12}]^a$ (cm^{-2})	$N_{H_2}[10^{20}]^{ab}$ (cm^{-2})	$M_{H_2}^{abc}$ ($M_\odot$)	$n_{H_2}^{abc}$ (cm^{-3})
	R1a	near : 3.9 far : 12.2	23.5	0.1	80	200	1.0×10^5 1.0×10^6	7.5×10^2 3.8×10^2
	R1c	near : 3.5 far : 12.6	-	-	> 2	> 5	$> 1.8 \times 10^3$ $> 2.4 \times 10^4$	$> 1.4 \times 10^1$ > 4
	R1e	near : 4.7 far : 11.4	-	-	> 13	> 31	$> 2.4 \times 10^4$ $> 1.4 \times 10^5$	$> 7.4 \times 10^1$ $> 3.0 \times 10^1$

NH_3	R1	distance (kpc)	$\tau_{NH_3(1,1)}$	T_{kin} (K)	N_{NH_3} $[10^{12}]$ (cm^{-2})	N_{H_2} $[10^{20}]^{ab}$ (cm^{-2})	$M_{H_2}^{abc}$ ($M_\odot$)	$n_{H_2}^{abc}$ (cm^{-3})
	R1a	near : 3.9 far : 12.2	0.43	18	46	46	1.4×10^4 9.7×10^4	2.0×10^2 6.3×10^1
	R1e	near : 4.7 far : 11.4	-	-	> 14	> 14	$> 6.1 \times 10^3$ $> 3.6 \times 10^4$	$> 4.8 \times 10^1$ $> 2.0 \times 10^1$

CO	R1	distance (kpc)	$M_{H_2}^d$ ($M_\odot$)	M_{vir} $(^{13}CO)^e$ ($M_\odot$)	$n_{H_2}^e$ (cm^{-3})
	R1a	near : 3.9 far : 12.2	1.2×10^5 1.1×10^6	$4.8 \times 10^4 - 2.1 \times 10^5$ $1.5 \times 10^5 - 5.3 \times 10^5$	9.6×10^2 3.0×10^2
	R1c	near : 3.5 far : 12.6	2.0×10^4 2.6×10^5	$6 \times 10^3 - 2.1 \times 10^4$ $2.1 \times 10^4 - 7.6 \times 10^4$	2.2×10^2 6.0×10^1
	R1d	near : 4.3 far : 11.8	6.8×10^3 5.2×104	$7.0 \times 10^3 - 2.6 \times 10^4$ $2.0 \times 10^4 - 7.1 \times 10^4$	4.3×10^1 1.5×10^1
	R1e	near : 4.7 far : 12.2	6.8×10^4 4.2×10^5	$1.5 \times 10^5 - 5.3 \times 10^5$ $7.8 \times 10^4 - 2.8 \times 10^5$	3.2×10^2 1.3×10^2

[a]:Parameters have been derived using the LTE assumption.
[b]:The H_2 physical parameters derived using a NH_3 abundance ratio $\chi_{NH_3} = 1 \times 10^{-8}$ and using a CS abundance ratio $\chi_{CS} = 4 \times 10^{-9}$.
[c]:H_2 mass and density from CS and NH_3 have been computed assuming the observed region is spherical or ellipsoid and whose size are given in table 2 and table 3.
[d]:H_2 mass are derived using a $X_{CO} = 2.0 \times 10^{20} cm^{-2}$ (K km/s)$^{-1}$ and assuming a spherical region.
[e]:Virial mass is computed using CO(1-0) and ^{13}CO(1-0) emission FWHM and assuming a spherical region. The left value represents the Virial mass for a $1/r^2$ density distribution whereas the right value indicate the value for a Gaussian distribution.
.

Table H1b. Parameters derived towards region *R2* using the molecular transition CS(1-0), CO(1-0), ^{13}CO(1-0), NH_3(1,1), NH_3(2,2) and $C^{34}S$(1-0) when emission are found. The labels *a,b,c,d* denote a distinct emission. Lower limits have been derived when we assumed $\tau = 0$

CS	R2	distance (kpc)	$\frac{W_{CS(1-0)}}{W_{C^{34}S(1-0)}}$	$\tau_{CS(1-0)}$	N_{CS} $[10^{12}]^a$ (cm^{-2})	$N_{H_2}[10^{20}]^{ab}$ (cm^{-2})	$M_{H_2}^{abc}$ ($M_\odot$)	$n_{H_2}^{abc}$ (cm^{-3})
	R2a	near : 4.0 far : 12.1	-	-	> 14	> 36	$> 3.4 \times 10^3$ $> 3.2 \times 10^4$	$> 3.3 \times 10^2$ $> 1.1 \times 10^2$
	R2e	near : 4.7 far : 11.4	13.3	1.5	100	250	3.4×10^4 2.0×10^5	2.0×10^3 8.5×10^2

NH_3	R2	distance (kpc)	$\tau_{NH_3(1,1)}$	T_{kin} (K)	N_{NH_3} $[10^{12}]$ (cm^{-2})	N_{H_2} $[10^{20}]^{ab}$ (cm^{-2})	$M_{H_2}^{abc}$ ($M_\odot$)	$n_{H_2}^{abc}$ (cm^{-3})
	R2a	near : 4.0 far : 12.1	-	-	> 5	> 5	$> 4.5 \times 10^2$ $> 4.0 \times 10^3$	$> 4.3 \times 10^1$ $> 1.4 \times 10^1$
	R2e	near : 4.7 far : 11.4	3.5	11	600	600	8.1×10^4 4.8×10^5	4.8×10^3 2.0×10^3

CO	R2	distance (kpc)	$M_{H_2}^d$ ($M_\odot$)	M_{vir} $(^{13}CO)^e$ ($M_\odot$)	$n_{H_2}^e$ (cm^{-3})
	R2a	near : 4.0 far: 12.1	1.3×10^4 1.1×10^5	$4.2 \times 10^3 - 2.5 \times 10^4$ $1.3 \times 10^4 - 4.4 \times 10^4$	1.2×10^3 8.9×10^2
	R2c	near : 3.5 far: 12.6	8.8×10^3 1.1×10^5	$8.9 \times 10^4 - 3.1 \times 10^5$ $3.2 \times 10^5 - 1.1 \times 10^6$	3.9×10^2 2.5×10^2
	R2e	near : 4.7 far: 11.4	2.9×10^4 2.0×10^5	$3.1 \times 10^4 - 1.1 \times 10^5$ $7.5 \times 10^4 - 2.7 \times 10^5$	1.7×10^3 6.4×10^2

[a]:Parameters have been derived using the LTE assumption.
[b]:The H_2 physical parameters derived using a NH_3 abundance ratio $\chi_{NH_3} = 1 \times 10^{-8}$ and using a CS abundance ratio $\chi_{CS} = 4 \times 10^{-9}$.
[c]:H_2 mass and density from CS and NH_3 have been computed assuming the observed region is spherical or ellipsoid and whose size are given in table 2 and table 3.
[d]:H_2 mass are derived using a $X_{CO} = 2.0 \times 10^{20} cm^{-2}$ (K km/s)$^{-1}$ and assuming a spherical region.
[e]:Virial mass is computed using CO(1-0) and ^{13}CO(1-0) emission FWHM and assuming a spherical region. The left value represents the Virial mass for a $1/r^2$ density distribution whereas the right value indicate the value for a Gaussian distribution.

Table H1c. Parameters derived towards region *R3* using the molecular transition CS(1-0), CO(1-0), ^{13}CO(1-0), NH_3(1,1), NH_3(2,2) and $C^{34}S$(1-0) when emission are found. The labels *a,b,c* denote a distinct emission. Lower limits have been derived when we assumed $\tau = 0$

CS	R3	distance (kpc)	$\frac{W_{CS(1-0)}}{W_{C^{34}S(1-0)}}$	$\tau_{CS(1-0)}$	N_{CS} $[10^{12}]^a$ (cm^{-2})	$N_{H_2}[10^{20}]^{ab}$ (cm^{-2})	$M_{H_2}^{abc}$ ($M_\odot$)	$n_{H_2}^{abc}$ (cm^{-3})
	R3e	near : 4.8 far : 11.3	-	-	> 7	> 16	$> 2.5 \times 10^2$ $> 1.7 \times 10^3$	$> 2.0 \times 10^2$ $> 1.1 \times 10^2$
	R3f	near : 2.9 far : 13.3	8.3	3.0	520	1300	7.4×10^3 1.5×10^5	3.5×10^4 7.6×10^3

NH_3	R3	distance (kpc)	$\tau_{NH_3(1,1)}$	T_{kin} (K)	N_{NH_3} $[10^{12}]$ (cm^{-2})	N_{H_2} $[10^{20}]^{ab}$ (cm^{-2})	$M_{H_2}^{abc}$ ($M_\odot$)	$n_{H_2}^{abc}$ (cm^{-3})
	R3f	near : 2.9 far : 13.3	2.0	20	165	165	9.5×10^2 1.3×10^4	4.4×10^3 6.2×10^2

CO	R3	distance (kpc)	$M_{H_2}^d$ ($M_\odot$)	M_{vir} $(^{13}CO)^e$ ($M_\odot$)	$n_{H_2}^e$ (cm^{-3})
	R3a	near : 2.9 far : 13.3	3.3×10^3 7.2×10^4	$1.2 \times 10^3 - 4.4 \times 10^3$ $5.7 \times 10^3 - 2.0 \times 10^4$	1.6×10^4 4.3×10^3
	R3e	near : 4.8 far : 11.3	2.3×10^3 1.3×10^4	$2.7 \times 10^3 - 9.6 \times 10^3$ $6.4 \times 10^4 - 2.3 \times 10^5$	2.5×10^3 1.1×10^3
	R3f	near : 3.8 far : 12.3	1.4×10^3 1.5×10^4	$2.1 \times 10^3 - 7.6 \times 10^3$ $6.9 \times 10^3 - 2.5 \times 10^4$	3.1×10^3 9.3×10^2

[a]:Parameters have been derived using the LTE assumption.
[b]:The H_2 physical parameters derived using a NH_3 abundance ratio $\chi_{NH_3} = 1 \times 10^{-8}$ and using a CS abundance ratio $\chi_{CS} = 4 \times 10^{-9}$.
[c]:H_2 mass and density from CS and NH_3 have been computed assuming the observed region is spherical or ellipsoid and whose size are given in table 2 and table 3.
[d]:H_2 mass are derived using a $X_{CO} = 2.0 \times 10^{20} cm^{-2}$ (K km/s)$^{-1}$ and assuming a spherical region.
[e]:Virial mass is computed using CO(1-0) and ^{13}CO(1-0) emission FWHM and assuming a spherical region. The left value represents the Virial mass for a $1/r^2$ density distribution whereas the right value indicate the value for a Gaussian distribution.

Table H1d. Parameters derived towards region *R4* using the molecular transition CS(1-0), CO(1-0), ^{13}CO(1-0), NH_3(1,1), NH_3(2,2) and $C^{34}S$(1-0) when emission are found. The labels *a*,*b*,*c* denote a distinct emission. Lower limits have been derived when we assumed $\tau = 0$

CS	R4	distance (kpc)	$\frac{W_{CS(1-0)}}{W_{C^{34}S(1-0)}}$	$\tau_{CS(1-0)}$	N_{CS} $[10^{12}]^a$ (cm^{-2})	$N_{H_2}[10^{20}]^{ab}$ (cm^{-2})	$M^{abc}_{H_2}$ ($M_\odot$)	$n^{abc}_{H_2}$ (cm^{-3})
	R4a	near : 4.0 far : 12.2	-	-	> 23	> 58	$> 7.4 \times 10^3$ $> 7.0 \times 10^4$	$> 4.1 \times 10^2$ $> 1.4 \times 10^2$
	R4b	near : 3.6 far : 12.5	-	-	> 15	> 38	$> 5.0 \times 10^3$ $> 4.9 \times 10^4$	$> 2.7 \times 10^2$ $> 9.0 \times 10^1$

NH_3	R4	distance (kpc)	$\tau_{NH_3(1,1)}$	T_{kin} (K)	N_{NH_3} $[10^{12}]$ (cm^{-2})	N_{H_2} $[10^{20}]^{ab}$ (cm^{-2})	$M^{abc}_{H_2}$ ($M_\odot$)	$n^{abc}_{H_2}$ (cm^{-3})
	R4a	near : 4.0 far : 12.2	-	-	> 19	> 19	$> 2.0 \times 10^3$ $> 2.4 \times 10^4$	$> 1.5 \times 10^2$ $> 4.4 \times 10^1$
	R4b	near : 3.6 far : 12.5	-	-	> 10	> 10	$> 1.2 \times 10^3$ $> 1.1 \times 10^4$	$> 7.0 \times 10^1$ $> 2.3 \times 10^1$

CO	R4	distance (kpc)	$M^d_{H_2}$ ($M_\odot$)	M_{vir} $(^{13}CO)^e$ ($M_\odot$)	$n^e_{H_2}$ (cm^{-3})
	R4a	near : 4.0 far : 12.2	1.6×10^4 1.5×10^5	$7.2 \times 10^3 - 2.5 \times 10^4$ $2.2 \times 10^4 - 7.8 \times 10^4$	9.3×10^2 3.0×10^2
	R4b	near : 3.6 far : 12.5	1.1×10^4 1.3×10^5	$6.1 \times 10^3 - 2.2 \times 10^4$ $2.1 \times 10^4 - 7.5 \times 10^4$	8.2×10^2 2.5×10^2
	R4e	near : 4.6 far : 11.5	9.0×10^3 5.6×10^4	$1.9 \times 10^4 - 6.7 \times 10^4$ $4.7 \times 10^4 - 1.7 \times 10^5$	3.6×10^2 1.1×10^2

[a]:Parameters have been derived using the LTE assumption.
[b]:The H_2 physical parameters derived using a NH_3 abundance ratio $\chi_{NH_3} = 1 \times 10^{-8}$ and using a CS abundance ratio $\chi_{CS} = 4 \times 10^{-9}$.
[c]:H_2 mass and density from CS and NH_3 have been computed assuming the observed region is spherical or ellipsoid and whose size are given in table 2 and table 3.
[d]:H_2 mass are derived using a $X_{CO} = 2.0 \times 10^{20} cm^{-2}$ (K km/s)$^{-1}$ and assuming a spherical region.
[e]:Virial mass is computed using CO(1-0) and ^{13}CO(1-0) emission FWHM and assuming a spherical region. The left value represents the Virial mass for a $1/r^2$ density distribution whereas the right value indicate the value for a Gaussian distribution.

Table H1e. Parameters derived towards region *R5* using the molecular transition CS(1-0), CO(1-0), ^{13}CO(1-0), NH_3(1,1), NH_3(2,2) and $C^{34}S$(1-0) when emission are found. The labels *a,b,c* denote a distinct emission. Lower limits have been derived when we assumed $\tau = 0$

CS	R5	distance (kpc)	$\frac{W_{CS(1-0)}}{W_{C^{34}S(1-0)}}$	$\tau_{CS(1-0)}$	N_{CS} $[10^{12}]^a$ (cm^{-2})	$N_{H_2}[10^{20}]^{ab}$ (cm^{-2})	$M_{H_2}^{abc}$ ($M_\odot$)	$n_{H_2}^{abc}$ (cm^{-3})
	R5a	near : 4.0 far : 12.1	-	-	> 3	> 7	$> 7.4 \times 10^2$ $> 6.7 \times 10^3$	$> 5.7 \times 10^1$ $> 1.9 \times 10^1$
	R5b	near : 3.7 far : 12.4	-	-	> 8	> 21	$> 1.8 \times 10^3$ $> 2.1 \times 10^4$	$> 1.9 \times 10^2$ $> 5.5 \times 10^1$

NH_3	R5	distance (kpc)	$\tau_{NH_3(1,1)}$	T_{kin} (K)	N_{NH_3} $[10^{12}]$ (cm^{-2})	N_{H_2} $[10^{20}]^{ab}$ (cm^{-2})	$M_{H_2}^{abc}$ ($M_\odot$)	$n_{H_2}^{abc}$ (cm^{-3})
	R5b	near : 3.7 far : 12.4	-	-	> 21	> 21	$> 2.0 \times 10^3$ $> 2.1 \times 10^4$	$> 1.9 \times 10^2$ $> 5.6 \times 10^1$

CO	R5	distance (kpc)	$M_{H_2}^d$ ($M_\odot$)	M_{vir} $(^{13}CO)^e$ ($M_\odot$)	$n_{H_2}^e$ (cm^{-3})
	R5a	near : 3.7 far : 12.4	9.5×10^3 1.1×10^4	$3.8 \times 10^4 - 1.4 \times 10^5$ $1.3 \times 10^5 - 4.6 \times 10^5$	6.8×10^2 2.0×10^2
	R5b	near : 4.0 far : 12.1	1.1×10^4 1.0×10^5	$1.5 \times 10^4 - 5.4 \times 10^4$ $4.6 \times 10^4 - 1.6 \times 10^5$	6.1×10^2 1.9×10^2
	R5c	near : 4.5 far : 11.6	3.4×10^3 2.3×10^4	$3.7 \times 10^4 - 1.3 \times 10^5$ $8.0 \times 10^4 - 2.9 \times 10^5$	1.4×10^2 5.0×10^1

[a]:Parameters have been derived using the LTE assumption.
[b]:The H_2 physical parameters derived using a NH_3 abundance ratio $\chi_{NH_3} = 1 \times 10^{-8}$ and using a CS abundance ratio$\chi_{CS} = 4 \times 10^{-9}$.
[c]:H_2 mass and density from CS and NH_3 have been computed assuming the observed region is spherical or ellipsoid and whose size are given in table 2 and table 3.
[d]:H_2 mass are derived using a $X_{CO} = 2.0 \times 10^{20} cm^{-2}$ (K km/s)$^{-1}$ and assuming a spherical region.
[e]:Virial mass is computed using CO(1-0) and ^{13}CO(1-0) emission FWHM and assuming a spherical region. The left value represents the Virial mass for a $1/r^2$ density distribution whereas the right value indicate the value for a Gaussian distribution.

Table H1f. Parameters derived towards region *R5* using the molecular transition CS(1-0), CO(1-0), ^{13}CO(1-0), NH_3(1,1), NH_3(2,2) and $C^{34}S$(1-0) when emission are found. Lower limits have been derived when we assumed $\tau = 0$

CS	R6	distance (kpc)	$\frac{W_{CS(1-0)}}{W_{C^{34}S(1-0)}}$	$\tau_{CS(1-0)}$	N_{CS} $[10^{12}]^a$ (cm^{-2})	$N_{H_2}[10^{20}]^{ab}$ (cm^{-2})	$M^{abc}_{H_2}$ ($M_\odot$)	$n^{abc}_{H_2}$ (cm^{-3})
	R6	near : 3.7 far : 12.5	-	-	> 30	> 75	$> 3.6 \times 10^4$ $> 4.2 \times 10^5$	$> 2.2 \times 10^2$ $> 6.5 \times 10^1$

CO	R6	distance (kpc)	$M^d_{H_2}$ ($M_\odot$)	M_{vir} $(^{13}CO)^e$ ($M_\odot$)	$n^e_{H_2}$ (cm^3)
	R6b	near : 3.7	7.6×10^4	$2.2 \times 10^4 - 7.9 \times 10^4$	4.3×10^2
		far : 12.5	8.7×10^5	$7.6 \times 10^4 - 2.7 \times 10^5$	1.7×10^2

[a]:Parameters have been derived using the LTE assumption.
[b]:The H_2 physical parameters derived using a NH_3 abundance ratio $\chi_{NH_3} = 1 \times 10^{-8}$ and using a CS abundance ratio $\chi_{CS} = 4 \times 10^{-9}$.
[c]:H_2 mass and density from CS and NH_3 have been computed assuming the observed region is spherical or ellipsoid and whose size are given in table 2 and table 3.
[d]:H_2 mass are derived using a $X_{CO} = 2.0 \times 10^{20} cm^{-2}$ (K km/s)$^{-1}$ and assuming a spherical region.
[e]:Virial mass is computed using CO(1-0) and ^{13}CO(1-0) emission FWHM and assuming a spherical region. The left value represents the Virial mass for a $1/r^2$ density distribution whereas the right value indicate the value for a Gaussian distribution.